Master thesis in mathematics

Applied and computational mathematics

Analysis of non-linear shallow water equations discretized on Arakawa C-grids

By: Espen Knudsen Eidsvåg
Supervisor: Jarle Berntsen

Spring 2016

Acknowledgements

This thesis was carried out at the Mathematical Institute of Bergen.

First of all i would like to thank my supervisor Jarle Berntsen for the support and guidance in this project. The conversations and feedback have been interesting as we explored different topics. Furthermore, I would like to thank the students, the professors and the staff I have met over the years at the Mathematical Institute and the Geophysical Institute of Bergen. The conversations and lectures have been insightful and helpful along the way. I also want to thank friends and family who have supported me in writing this thesis.

This thesis would not have been possible without the help from all of you.

Abstract

To model the behaviour of flow and waves in three dimensions, one may use the Navier-Stokes equations. These equations leads to the shallow water equations, when the depth is much smaller than the wavelength. The shallow water equations are depth-integrated Navier-Stokes equations, and they depict in general a two dimensional wave which can not vary with the depth. Storm surges and tidal waves are described by the shallow water equations. When we want to make a forecast of these waves, it is beneficial to use shallow water equations discretized on a Arakawa C-grid. Fourier methods have been used to study the stability of the solutions for constant depths. In this master thesis, we will study the stability of numerical methods for solving the shallow water equations, investigating the eigenvalues of the propagation matrices of a few grid cells. The effects of variable depths and non-linear terms are addressed. For the constant depths cases, the eigenvalues are purely imaginary. In the non-linear cases, the eigenvalues may have non-zero real components, which may give growth or damping of the solutions. By building on the two-cell case, the three- and the four-cell cases are explored in detail. With the three-cell case we introduce the non-linear term, which have the potential to change the stability.

For this case, we show a skew-symmetric form for the non-linear shallow water equations by combining the flux and advective forms in the three cell case. This form does not work on variable depths. The four-cell case is discussed to great extent, as it is set up differently than the two- and three-cell case. The behaviour of the eigenvalues have been important to study the stability of the cases. To understand the modes of the cases, the eigenvectors have been interpreted. The condition of skew-symmetry for the non-linear variable depths cases might be a too strong restriction, as the modes do not disperse to different frequencies. This is contrary to the behaviour of real waves, where we have interaction between different modes.

Contents

Chapter 1

Introduction

Gravity waves are created by gravitational pull on bodies of water, one example is tidal waves. When studying the dynamics of tides and storm surges, one may apply the shallow water equations to model the motion of the waves. The ocean models based on discretization of the shallow water equations are used to study tidal effects and the effects of surface elevation and currents. Forecasting systems for tides are based on such models.

The shallow water equations are derived from the Navier-Stokes equations, by depth-integrating the equations, under the assumption that the horizontal length scale is much larger than the vertical scale. To discretize the shallow water equations, it is an advantage to use staggered Arakawa grids. There are various Arakawa grids, from the A- to the E-grid, each of these is a different way of positioning the dependent variables of horizontal velocities and surface elevation. In our study we will use the C-grid, shown in Fig.1.1. The C-grid has the surface elevation in the middle of the grid and horizontal velocities on the boundary edges. According to studies from (Arakawa and Lamb, 1977), the Arakawa C-grid is the preferred to use when the Rossby radius of deformation is larger than the grid size .

In this thesis, a few cell approach will be applied to analyse classic discretization methods of the shallow water equations. For systems consisting of a few discrete cells, the eigenvalues and the eigenvectors will be computed and the stability of the discretization method analysed. Analysis of the shallow water equations has been done extensively with Fourier methods, but these methods assume constant depths and linear systems. In the master degree project I will investigate non-linear systems, I will do so by studying few cells so that the eigenvalues and eigenvectors are accurately calculated. In chapter 2 the two-cell case will be discussed, laying out the foundation of the the way forward. Then we study the three-cell case in chapter 3, where we will introduce different depths in the model. In chapter 4 we add the non-linear term to the three cell and analyse the effect it has. Chapter 5 will pertain a method to make the non-linear term more stable in the three-cell case for constant depths. The next chapter, chapter 6, goes into the four-cell case, making extensive studies of the various modes it contains. The effects the non-linear terms have on the four-cell case are discussed in chapter 7. At the end of the thesis, a discussion of results and ideas for further research are given.

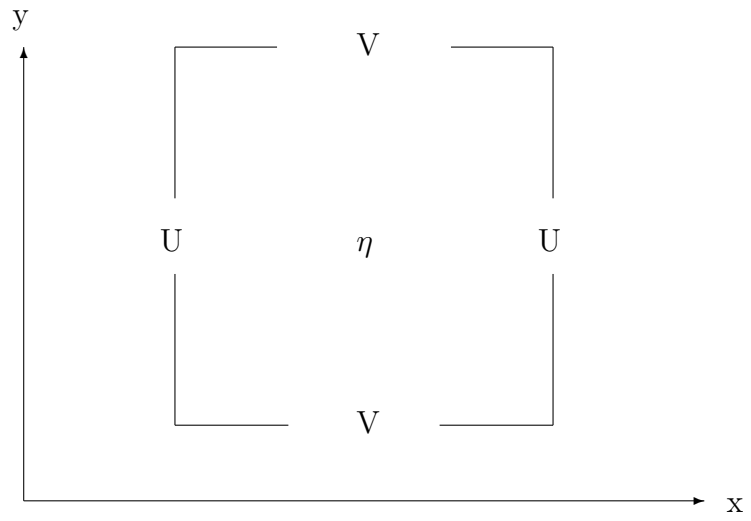

Figure 1.1: The variables in a staggered Arakawa C-grid, the depth-averaged velocity components in the x-direction, U, and the y-direction, V, are given at the edge midpoints of the computational grid. The surface elevation, η, is located in the center of the computational grid. The undisturbed mean depth H is given at the velocity points.

1.1 Motivation

In this study, we will start with modelling gravity waves in simple Arakawa C-grids, starting with the most basic units and increasing the complexity by adding cells and terms to the governing equations. We will discuss the stability and energy of the various cases. Furthermore, we will search for a way to weight the system of equations, so that the propagation matrix becomes similar to a skew-symmetric matrix. In (Espelid et al., 2000), this was a stated goal for further research.

1.2 The Navier-Stokes equations

This derivation is a modified version of the proof in (Reddy, 2013). The Navier-Stokes equations are derived from the momentum equations

$$\rho \frac{D\mathbf{u}}{Dt} = \nabla \cdot \sigma + \mathbf{f} \,.$$

Where ρ is the density of the fluid, $\mathbf{u}$ is the velocity vector, σ the stress tensor and $\mathbf{f}$ the body force vector, typically gravity. The momentum equation gives the balance of momentum transport in a continuous body. If we assume the linear elastic constitutive equations, then the stress tensor can be decomposed into the deviatoric stress tensor ($\tau = \mu(\nabla \mathbf{u} + (\nabla \mathbf{u})^T)$), the volume viscosity tensor $\zeta(\nabla \cdot \mathbf{u})I$ and the pressure tensor PI. Where μ is dynamic viscosity, ζ is the volume viscosity, and P is the pressure. Thus, we are left with the compressible Navier-Stokes equations

$$\rho \frac{D\mathbf{u}}{Dt} = \mu \Delta \mathbf{u} + \zeta \nabla(\nabla \cdot \mathbf{u}) - \nabla P + \mathbf{f} \,.$$

The volume viscosity ζ comes into action if we have sudden change in volume, as in a sound shock. Otherwise, when we have incompressible fluid ($\nabla \cdot \mathbf{u} = 0$), which is approximately true with water, we get the familiar incompressible Navier-Stokes equations

$$\rho \frac{D\mathbf{u}}{Dt} = \mu \Delta \mathbf{u} - \nabla P + \mathbf{f} \,. \tag{1.1}$$

1.3 Shallow water equations

The shallow water equations are derived from the Navier-Stokes equations by depth-integration. We start with the horizontal velocity vector $\mathbf{u}$, which we decompose into the sum of a depth-averaged component $\mathbf{U}$, and depth-varying component $\mathbf{u}'$. Likewise, the total depth h is decomposed into a sum of surface elevation η and mean depth H. The hydrostatic pressure P omits the atmospheric pressure, depending only on gravity g, surface elevation η, and ignoring density variation.

$$\mathbf{u}(x,y,z,t) = \mathbf{U}(x,y,t) + \mathbf{u}'(x,y,z,t)\,,\; h(x,y,t) = H(x,y) + \eta(x,y,t)\,,$$

$$\int_{-H}^{\eta} -\frac{\mathbf{u}}{h} dz = \mathbf{U}\,, P = \rho g \eta.$$

Depth integration of the Navier-Stokes equations (Eqn.1.1), and setting the dynamic viscosity to 0 and dividing by the density ρ, will give us

$$\int_{-H}^{\eta} (\frac{D\mathbf{u}}{Dt} + fk \times \mathbf{u} + \nabla p) dz = 0\,.$$

The body force is represented here by the Coriolis pseudo-force $\rho f \mathbf{k} \times \mathbf{u}$, and the stress by the pressure gradient force ∇p, where $p = g\eta$. By performing the integral, we get the following equations

$$\frac{D(h\mathbf{U})}{Dt} + fh\mathbf{k} \times \mathbf{U} + gh\nabla\eta = 0\,,$$

$$\frac{D(\mathbf{U})}{Dt} + f\mathbf{k} \times \mathbf{U} + g\nabla\eta = 0\,.$$

The kinematic and surface boundary conditions give us the last part of the depth-integrated shallow water equations

$$\frac{\partial \eta}{\partial t} + \nabla \cdot (h\mathbf{U}) = 0\,.$$

We have omitted the non-linear terms here as well. This was a simplified version of the derivation in the book (Haidvogel and Beckmann, 1999).

The shallow water equations form a basis for studies of storm surges and tidal waves. They are discretized in space and time by numerical models, and these models have been investigated in many studies. For this master thesis we will not include the Coriolis effect in the equations, but we will include non-linear terms in this general set of equations

$$\begin{aligned} \frac{\partial U}{\partial t} + U\frac{\partial U}{\partial x} + V\frac{\partial U}{\partial y} + g\frac{\partial \eta}{\partial x} &= 0\,, \\ \frac{\partial V}{\partial t} + U\frac{\partial V}{\partial x} + V\frac{\partial V}{\partial y} + g\frac{\partial \eta}{\partial y} &= 0\,, \\ \frac{\partial \eta}{\partial t} + \frac{\partial (HU)}{\partial x} + \frac{\partial (HV)}{\partial y} &= 0\,. \end{aligned} \tag{1.2}$$

The last equation, produced from the kinematic and boundary conditions, omits the surface elevation component η of the total depth h. This component, η, is in general significantly smaller than the mean depth. Throughout the paper we will find different forms of discretization, but they all end up with a propagation matrix, and we will use the trapezoidal scheme to iterate for each time step. The grid we choose to use in this thesis, is the staggered Arakawa C-grid, as shown in Fig.1.1. Staggered grids are useful to avoid decoupling of the variables. In addition, they do not smooth the solutions with the differential operators, as normal grids would do.

1.4 Seiches

Seiches are standing waves in an enclosed or an almost enclosed body of water. The seiches appear when the wind or the tidal pull have the right frequencies. That is, the frequencies that resonate with the geometry of the body of water. There can be multiple patterns of the standing waves that have this property in the closed body and we call each of these patterns a mode. Studies have been made on various scales of seiches. We can find seiches at the coast, as harbour oscillation portrayed in (Rabinovich, 2009). This study also gives periods of the modes, belonging to various simple geometries of the basins. On a greater scale, Lake Zurich is an example of a body of water that is on the scale of the Rossby radius of deformation, seiches occur frequently there. The scales of the standing waves are larger as well, the winds have to be stronger and longer to resonate with the eigenfrequencies of the lake. Further details are given in (Horn et al., 1986). Signs of Kelvin waves are also mentioned in the paper. When the size of the body of water is larger than the Rossby radius of deformation, the Coriolis effect begins to be important. On a scale that spans multiple latitudes, we have the Baltic sea. The Baltic Sea is approximately an enclosed body of water with a small outlet into the Atlantic Ocean. The paper by (Wubber and Krauss, 1979), gives us an understanding of the modes in the Baltic Sea, and illustrates the effect the Coriolis parameter has on the modes.

1.5 Method of approach

As previously noted, Fourier methods are used to investigate stability and energy conservation, but can not be used when adding non-linear terms to the shallow water equations. We have the Gibbs phenomenon as well, when we have different depths of the grid cells. The approach will rather be to manage the real part of the eigenvalues, and to design numerical schemes that minimize the numerical error growth. The method will be to study the eigenvalues of these schemes on a small scale using Arakawa C-grid cells, popular with ocean circulation models. Expanding the complexity will be done by introducing more cells, non-linearity and distinctly different depths at the velocity points in the grid cells. It can be shown that the phase errors of the waves affected by rotation, may be reduced by using staggered C-grids see (Haidvogel and Beckmann, 1999).

Chapter 2

The two-cell case

The two-cell case is a simple starting point to begin understanding the shallow water equations in staggered grids. For the two-cell case using the Arakawa C-grid, there is three variables, see Fig.2.1.

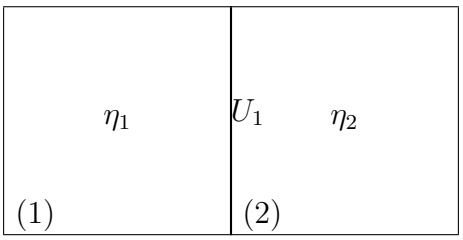

Figure 2.1: The variables of the two-cell case. The cells are numbered 1 to 2.

In this figure, U_1 is the depth-averaged velocity in the x-direction, η_1 and η_2 are the surface elevations at the center of each cell, and H the undisturbed mean water depth at the U_1-point. The depth-averaged velocity components in the y-direction are 0. If we neglect the non-linear term from Eqn.1.2, the shallow water equations in the two-cell case are

$$\begin{aligned} \frac{\partial U}{\partial t} &= -g\frac{\partial \eta}{\partial x}\,, \\ \frac{\partial \eta}{\partial t} &= -\frac{\partial (HU)}{\partial x}\,. \end{aligned} \tag{2.1}$$

Discretizing these equations in space only, assuming closed boundaries and a quadratic grid size of Δx, the following system of ordinary differential equations (ODE's) is obtained

$$\begin{aligned} \frac{dU_1}{dt} &= -g\frac{\eta_2 - \eta_1}{\Delta x}\,, \\ \frac{d\eta_1}{dt} &= -H\frac{U_1}{\Delta x}\,, \\ \frac{d\eta_2}{dt} &= H\frac{U_1}{\Delta x}\,. \end{aligned} \tag{2.2}$$

The boundary velocities are set to zero. The system of equations can be put as a matrix equation with setting

$$\mathbf{w}(t) = \begin{pmatrix} U_1(t) \\ \eta_1(t) \\ \eta_2(t) \end{pmatrix},$$

and the whole system as

$$\frac{d}{dt}\mathbf{w}(t) = A\mathbf{w}(t)\,. \tag{2.3}$$

From Eqn.2.2 we obtain the elements of A

$$A = \begin{pmatrix} 0 & \frac{g}{\Delta x} & -\frac{g}{\Delta x} \\ -\frac{H}{\Delta x} & 0 & 0 \\ \frac{H}{\Delta x} & 0 & 0 \end{pmatrix} .$$

The matrix A is time independent. It will have constant eigenvalues that are roots of the equation

$$det(A - \lambda I) = \begin{vmatrix} -\lambda & \frac{g}{\Delta x} & -\frac{g}{\Delta x} \\ -\frac{H}{\Delta x} & -\lambda & 0 \\ \frac{H}{\Delta x} & 0 & -\lambda \end{vmatrix} = 0 .$$

We retrieve the characteristic equation

$$-\lambda^3 - \frac{2gH\lambda}{(\Delta x)^2} = 0 . \tag{2.4}$$

The eigenvalues are then

$$\lambda_0 = 0 , \lambda_{1,2} = \pm i\frac{\sqrt{2gH}}{\Delta x} .$$

Meriam's formula of a standing wave in a closed body is

$$T = \frac{2\pi}{w} = \frac{2L}{\sqrt{gH}} .$$

Where T is the period, w the angular frequency, L is the length of the body and H is the average depth of the body. The allowable angular frequencies in the continuous case is

$$w = \frac{\pi(n+1)}{L}\sqrt{gH}, \quad n = 0, 1, 2, ... \tag{2.5}$$

in this formula, n is the wave mode number and the constant $\pi \approx 3.14$. Discussion of various modes will be a subject throughout the paper, so it is an important formula. Since our model is discrete, we will have a different angular frequency, and we can check the difference by rewriting the discrete case angular frequency to see this more clearly

$$w = \frac{\sqrt{2gH}}{\Delta x} = \frac{2\sqrt{2gH}}{2\Delta x} = \frac{2\sqrt{2}\sqrt{gH}}{L} .$$

Two times the root of two, which is close to π. We will do this procedure for the three cell case as well. The corresponding eigenvectors to the eigenvalues are

$$\mathbf{x}_0 = \begin{pmatrix} 0 \\ 1 \\ 1 \end{pmatrix} , \mathbf{x}_{1,2} = \begin{pmatrix} \pm i\sqrt{2gH} \\ -H \\ H \end{pmatrix} .$$

These eigenvalues are used in the general solution as a scalar combination multiplied with the exponential of the corresponding eigenvalues

$$\mathbf{w}(t) = d_0\mathbf{x}_0 e^{\lambda_0 t} + d_1\mathbf{x}_1 e^{\lambda_1 t} + d_2\mathbf{x}_2 e^{\lambda_2 t} , \tag{2.6}$$

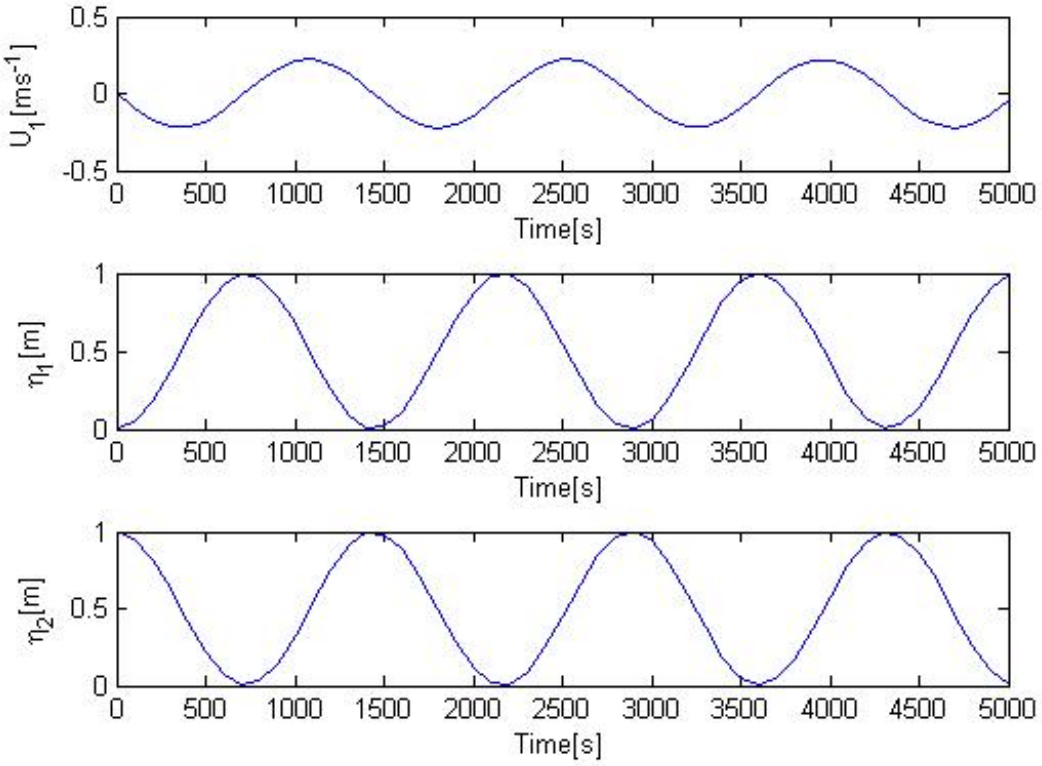

Figure 2.2: Time series of the exact solution for Eqn.2.7.

where d_0, d_1 and d_2 are constant coefficients and t is the independent variable of time. The eigenvector $\mathbf{x}_0$ gives the steady state solution with zero depth-averaged velocity, when used as initial values. When $d_2, d_3 = 0$ we have an equilibrium, since the depth-averaged velocity $U_1 = 0ms^{-1}$ and there is no difference in the surface elevations, $\eta_1 = \eta_2$. The $\mathbf{x}_1$, $\mathbf{x}_2$ eigenvectors represents the situations where we have a gravity wave with a corresponding angular frequency. Regarding the non-trivial waves, our model only has an angular frequency of $\frac{\sqrt{2gH}}{\Delta x}$. The standing wave that this solution represent is only physically possible if the wavelength is one of the modes $\lambda_n = \frac{2L}{n+1}$. In our case we have $L = 2\Delta x$ and the mode $\lambda_1 = \frac{2L}{2} = 2\Delta x$, this mode has a fixed point in the middle of the two cell, see-sawing back and forth.

If we set the initial conditions $U_1(0) = 0ms^{-1}$, $\eta_1(0) = 0m$, $\eta_2(0) = 1m$, the initial vector is

$$\mathbf{w}(0) = \begin{pmatrix} 0 \\ 0 \\ 1 \end{pmatrix} .$$

Inserting these initial values in Eqn.2.6, the exact solutions for U, η_1, η_2 are

$$\begin{aligned} U_1(t) &= -\sqrt{\tfrac{g}{2H}} sin(\tfrac{\sqrt{2gH}}{\Delta x} t)\,, \\ \eta_1(t) &= \tfrac{1}{2} - \tfrac{1}{2} cos(\tfrac{\sqrt{2gH}}{\Delta x} t)\,, \\ \eta_2(t) &= \tfrac{1}{2} + \tfrac{1}{2} cos(\tfrac{\sqrt{2gH}}{\Delta x} t)\,, \end{aligned} \tag{2.7}$$

and the numerical solutions are given in Fig.2.2. The values of the constants are $H = 100m$ and $\Delta x = 10km$. This produces the exact solution an angular frequency of value $4.43 * 10^{-3} s^{-1}$, and a period of 1419s. This period is in agreement with the numerical period observed in Fig.2.2. For small linear systems of differential equations we have an exact solution, but for large non-linear systems we generally do not. Hence we resort to numerical solutions as the complexity increases. We will use the exact solution to check the quality of the numerical solution for our small linear case. The numerical method we will use to produce solutions of Eqn.2.7 is the trapezoidal scheme

$$\frac{\mathbf{w}^{(n+1)} - \mathbf{w}^{(n)}}{\Delta t} = \frac{A\mathbf{w}^{(n+1)} + A\mathbf{w}^{(n)}}{2} .$$

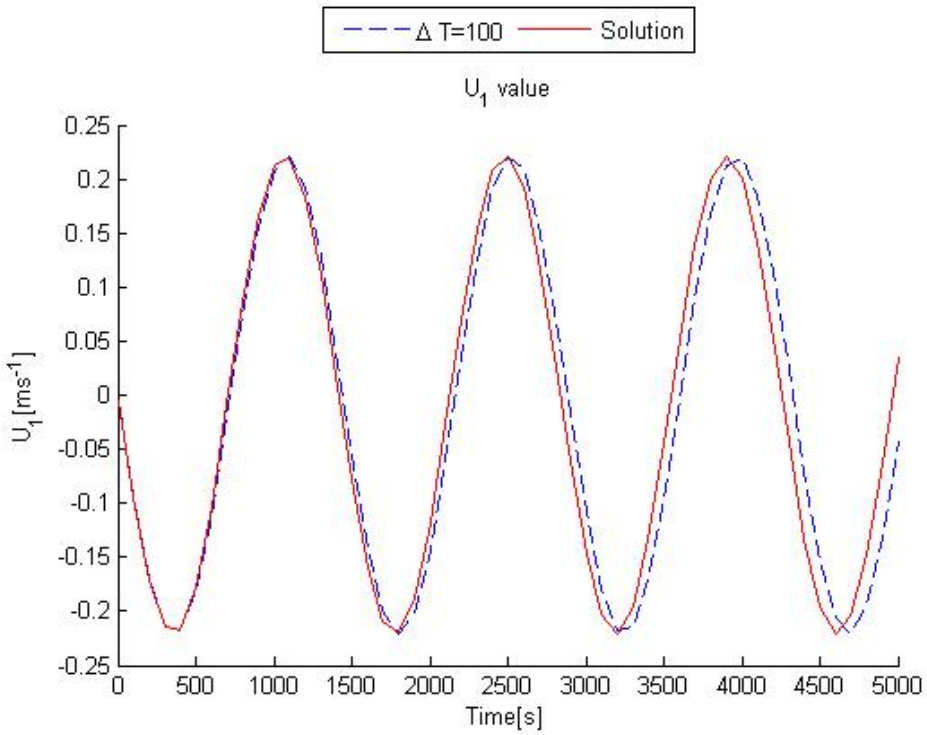

Figure 2.3: Time series of U_1, the exact solution is given by a solid red line and the numerical solution a dotted blue line with $\Delta t = 100s$

Solving for $\mathbf{w}^{(n+1)}$,

$$\mathbf{w}^{(n+1)} = \left(I - \frac{\Delta t}{2}A\right)^{-1}\left(I + \frac{\Delta t}{2}A\right)\mathbf{w}^{(n)}\,.$$

It can be shown that this scheme (Mesinger and Arakawa, 1976) preserves the amplitude of the oscillations, and that energy is conserved when applying this method. Next, we study the phase error of the method. When we have a large time step, the numerical solution will come out of phase, compared to the exact solution, as shown in Fig.2.3. Since the method is of second order, $O((\Delta t)^2)$, we may reduce Δt by a factor of 2, then the amplitude of the error becomes four times less, as shown in Fig.2.4. We want the error of the amplitude for the U_1 solution to be of the magnitude $10^{-3}ms^{-1}$, and we obtain this by setting the time step equal to $12.5s$, also shown in Fig.2.4. The time step size we will use from now on, throughout the paper, will be $\Delta t = 10s$. We will generally use 500 time steps, which produce a 5000s period. In this chapter we have studied the various properties of the shallow water equations discretized over two cells. The next chapter will build on these results, to help understand the three-cell case.

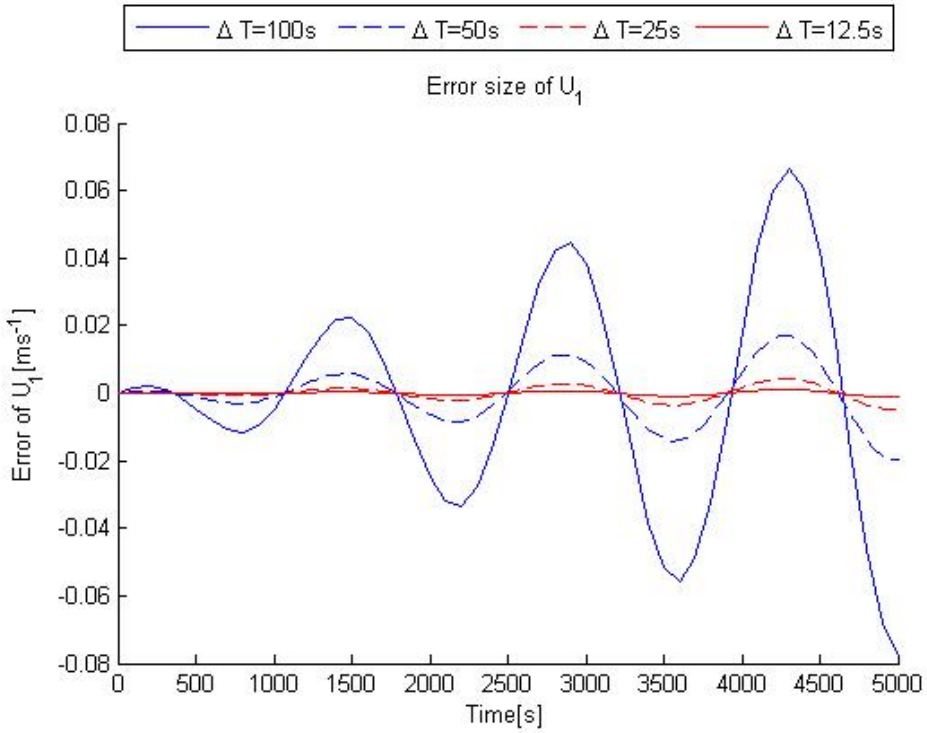

Figure 2.4: Errors compared to true solution, with three different time step sizes. For each time Δt doubles, one can compare the values between the oscillation peaks. The factor for each doubling is approximately 3.94.

Chapter 3

The linear three-cell case

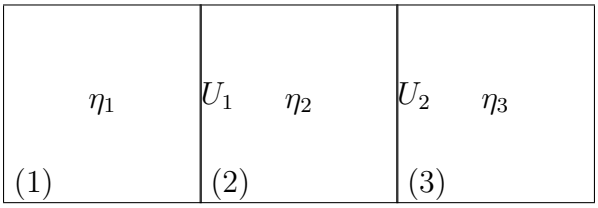

Figure 3.1: Variables in the three-cell case. The cells are numbered 1 to 3.

To further gain insight of the shallow water equations on Arakawa C-grid, we will expand the model with another cell. The three-cell case includes two depths and depth-averaged velocities making, it possible to include the non-linear term in the next chapter. In the three-cell case we have 5 variables, the depth-averaged velocities U_1 and U_2 as well as the surface elevations η_1 to η_3 centred in each cell, from cell 1 to cell 3, as shown in Fig.3.1. In addition we have two constants, the depths H_1 and H_2, at the U_1 and U_2 position and the grid distance Δx. If we set the grid cells quadratic, then the discretized shallow water equations are written in this case

$$\begin{aligned}
\frac{dU_1}{dt} &= -g\frac{\eta_2-\eta_1}{\Delta x}\,,\\
\frac{dU_2}{dt} &= -g\frac{\eta_3-\eta_2}{\Delta x}\,,\\
\frac{d\eta_1}{dt} &= -H_1\frac{U_1}{\Delta x}\,,\\
\frac{d\eta_2}{dt} &= H_1\frac{U_1}{\Delta x}-H_2\frac{U_2}{\Delta x}\,,\\
\frac{d\eta_3}{dt} &= H_2\frac{U_2}{\Delta x}\,.
\end{aligned} \tag{3.1}$$

The whole system of these ODE's can then be written compactly

$$\frac{d}{dt}\mathbf{w}(t) = \begin{pmatrix} 0 & 0 & \frac{g}{\Delta x} & -\frac{g}{\Delta x} & 0\\ 0 & 0 & 0 & \frac{g}{\Delta x} & -\frac{g}{\Delta x}\\ -\frac{H_1}{\Delta x} & 0 & 0 & 0 & 0\\ \frac{H_1}{\Delta x} & -\frac{H_2}{\Delta x} & 0 & 0 & 0\\ 0 & \frac{H_2}{\Delta x} & 0 & 0 & 0 \end{pmatrix} \mathbf{w}(t) = A\mathbf{w}(t)\,,$$

where

$$\mathbf{w}(t) = \begin{pmatrix} U_1(t) \\ U_2(t) \\ \eta_1(t) \\ \eta_2(t) \\ \eta_3(t) \end{pmatrix}.$$

We turn now to calculating the eigenvalues of the propagation matrix A from the expression

$$det(A - \lambda I) = \begin{vmatrix} -\lambda & 0 & \frac{g}{\Delta x} & -\frac{g}{\Delta x} & 0 \\ 0 & -\lambda & 0 & \frac{g}{\Delta x} & -\frac{g}{\Delta x} \\ -\frac{H_1}{\Delta x} & 0 & -\lambda & 0 & 0 \\ \frac{H_1}{\Delta x} & -\frac{H_2}{\Delta x} & 0 & -\lambda & 0 \\ 0 & \frac{H_2}{\Delta x} & 0 & 0 & -\lambda \end{vmatrix} = 0\,.$$

By evaluating the Laplacian expansion of the determinant along first row, we end up with the characteristic equation

$$-\lambda^5 - \frac{2g(H_1 + H_2)\lambda^3}{(\Delta x)^2} - \frac{3g^2 H_1 H_2 \lambda}{(\Delta x)^4} = 0\,.$$

When $H_2 = H_1 = H$, we get the five eigenvalues

$$\begin{aligned} \lambda_0 &= 0\,, \\ \lambda_{1,2} &= \pm\frac{i\sqrt{g}}{\Delta x}\sqrt{H}\,, \\ \lambda_{3,4} &= \pm\frac{i\sqrt{g}}{\Delta x}\sqrt{3H}\,. \end{aligned} \tag{3.2}$$

The absolute values for the last two sets of eigenvalues are non-zero, hence we will have oscillations with two different angular frequencies. We set the constant depth $H = 100m$. This is almost the same situation as the two-cell case, it is just extended by a grid cell. Thus, we end up with the angular frequencies $3.13 * 10^{-3} s^{-1}$ and $5.42 * 10^{-3} s^{-1}$ and the corresponding periods $2006s$ and $1158s$. These periods are longer and shorter than the single period in the two-cell case, so we should expect more complicated solutions than the two-cell case, which is verified by Fig.3.2. By taking the same initial values, we get a comparison of the two- and three-cell cases. This figure gives the solutions with the initial value $\eta_3 = 1m$, the only non-zero entry in the initial vector $\mathbf{w}(0)$. Furthermore, in Fig.3.2, we can check the calculated angular frequencies by observing the periods of the functions. The η_2 solution has a period of approximately 1100s, the η_1 and η_3 solutions have a period of about 2000s, which corresponds well with the calculated values. The corresponding eigenvectors to the eigenvalues are

$$\mathbf{x}_0 = \begin{pmatrix} 0 \\ 0 \\ 1 \\ 1 \\ 1 \end{pmatrix}, \mathbf{x}_{1,2} = \begin{pmatrix} \mp i\sqrt{gH} \\ \pm i\sqrt{gH} \\ -H \\ 0 \\ H \end{pmatrix}, \mathbf{x}_{3,4} = \begin{pmatrix} \mp i\sqrt{3gH} \\ \pm i\sqrt{3gH} \\ -H \\ 2H \\ -H \end{pmatrix}.$$

The eigenvalues rendered us the non-zero angular frequencies $w_1 = \frac{\sqrt{gH}}{\Delta x}$ and $w_2 = \frac{\sqrt{3gH}}{\Delta x}$. A check of the allowable angular frequencies from Merian's formula, gives that it is approximately equal to our discrete case

$$w = \frac{\pi(n+1)}{L}\sqrt{gH}\,,$$

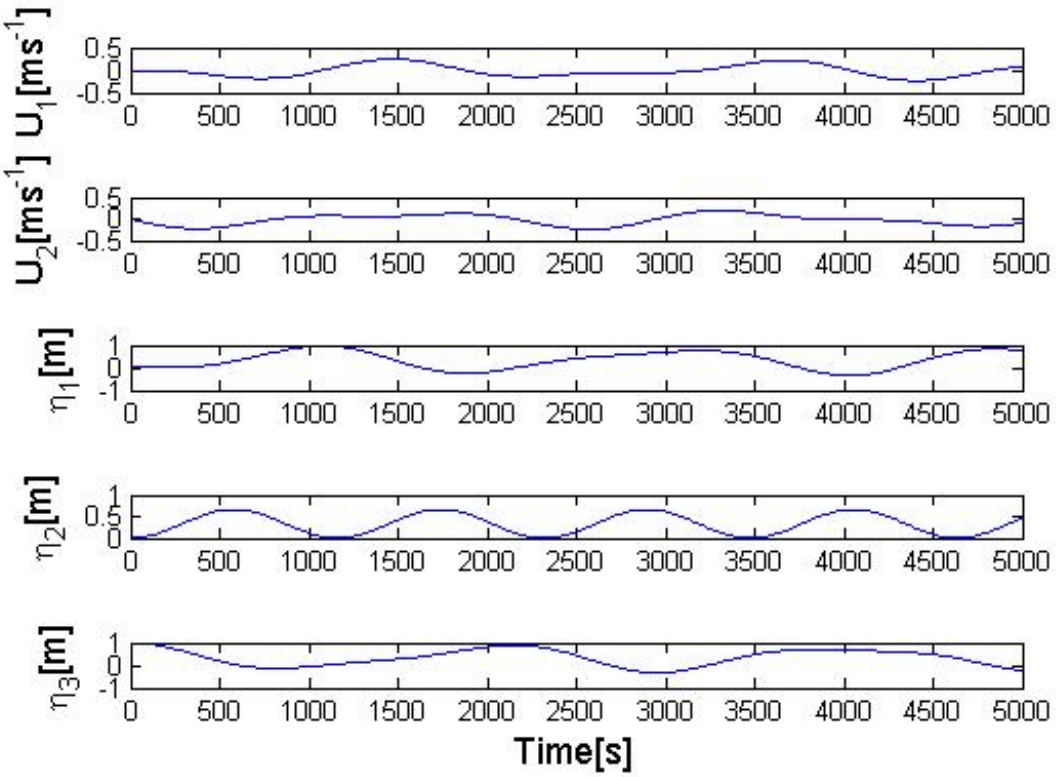

Figure 3.2: The numerical solution with $H_1, H_2 = 100m$ and $\eta_3 = 1m$, the rest of the initial values are zero.

$$w_1 = \frac{\sqrt{gH}}{\Delta x} = \frac{3\sqrt{gH}}{3\Delta x} = \frac{3\sqrt{gH}}{L} \approx \frac{\pi\sqrt{gH}}{L}\,,$$
$$w_2 = \frac{\sqrt{3gH}}{\Delta x} = \frac{3\sqrt{3gH}}{3\Delta x} = \frac{3\sqrt{3}\sqrt{gH}}{L} \approx \frac{2\pi\sqrt{gH}}{L}\,.$$

When $H_1 \neq H_2$, we have the five eigenvalues

$$\begin{aligned}
\lambda_0 &= 0\,,\\
\lambda_{1,2} &= \pm\frac{i\sqrt{g}}{\Delta x}\sqrt{H_1 + H_2 - \sqrt{H_1^2 - H_1H_2 + H_2^2}}\,,\\
\lambda_{3,4} &= \pm\frac{i\sqrt{g}}{\Delta x}\sqrt{H_1 + H_2 + \sqrt{H_1^2 - H_1H_2 + H_2^2}}\,,
\end{aligned} \tag{3.3}$$

with the corresponding five eigenvectors, where we set $s = \sqrt{H_1^2 - H_1H_2 + H_2^2}$,

$$\mathbf{x}_0 = \begin{pmatrix} 0\\0\\1\\1\\1 \end{pmatrix}\,, \mathbf{x}_{1,2} = \begin{pmatrix} \mp i\sqrt{g}\sqrt{H_1 + H_2 - s}\\ \frac{2H_2 - H_1 - 2s}{H_2 + H_1 - s}(\pm i\sqrt{g}\sqrt{H_1 + H_2 - s}\,)\\ -H_1\\ H_2 - s\\ H_1 - H_2 + s \end{pmatrix}\,,$$

$$\mathbf{x}_{3,4} = \begin{pmatrix} \mp i\sqrt{g}\sqrt{H_1 + H_2 + s}\\ \frac{2H_2 - H_1 + 2s}{H_2 + H_1 + s}(\pm i\sqrt{g}\sqrt{H_1 + H_2 + s}\,)\\ -H_1\\ H_2 + s\\ H_1 - H_2 - s \end{pmatrix}\,.$$

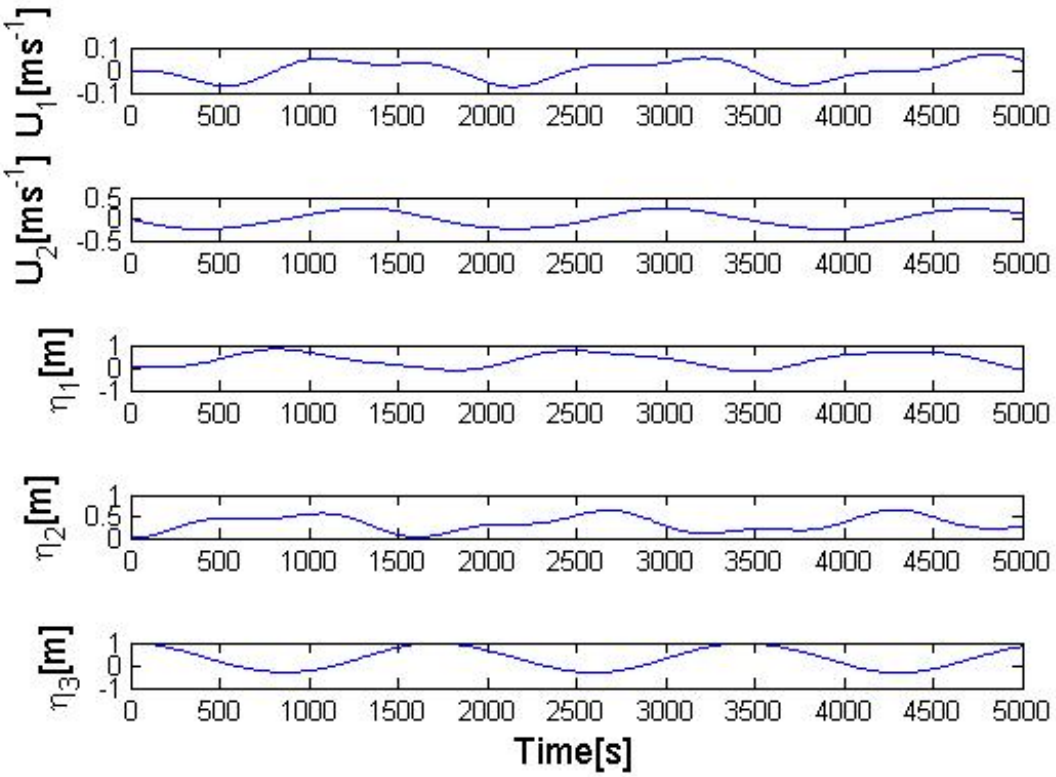

Figure 3.3: The numerical solution for the $H_1 = 100m$ and $H_2 = 300m$ case. Only the initial value $\eta_3 = 1m$ is non-zero from the start.

Portrayed in Fig.3.3, are the numerical solutions with variable depths, the initial vector being

$$\mathbf{w}(0) = \begin{pmatrix} 0 \\ 0 \\ 0 \\ 0 \\ 1 \end{pmatrix},$$

and the depths $H_1 = 100m$ and $H_2 = 300m$.

With these choices of the depths, we get the angular frequencies $8.07 * 10^{-3}s^{-1}$ and $3.64 * 10^{-3}s^{-1}$. The corresponding time periods of $779s$ and $1723s$ are both approximately $300s$ smaller than the constant depths case, so lowering the H_2 depth gives faster modes in our case. This can be proved by considering the eigenvalues

$$\lambda_{1,2,3,4} = \pm\frac{i\sqrt{g}}{\Delta x}\sqrt{H_1 + H_2 \pm \sqrt{H_1^2 - H_1H_2 + H_2^2}},$$

and setting $H_2 = H_1 + \Delta H$, we get

$$\lambda_{1,2,3,4} = \pm\frac{i\sqrt{g}}{\Delta x}\sqrt{2H_1 + \Delta H \pm \sqrt{H_1^2 + H_1\Delta H + (\Delta H)^2}}.$$

By setting these eigenvalues greater than $\frac{i\sqrt{g}}{\Delta x}\sqrt{H_1}$ or $\frac{i\sqrt{g}}{\Delta x}\sqrt{3H_1}$, we end up with a true inequality for all values of H_1 that is non-zero. Therefore, we will have faster or equal oscillations for all the eigenvalues in all cases with variable depths, in our case ΔH was 200m. If we have $\Delta H << H_1$, we obtain

$$\sqrt{H_1^2 + H_1\Delta H + (\Delta H)^2} \approx H_1,$$

giving us

$$\lambda_{1,2,3,4} \approx \pm\frac{i\sqrt{g}}{\Delta x}\sqrt{2H_1 \pm H_1},$$

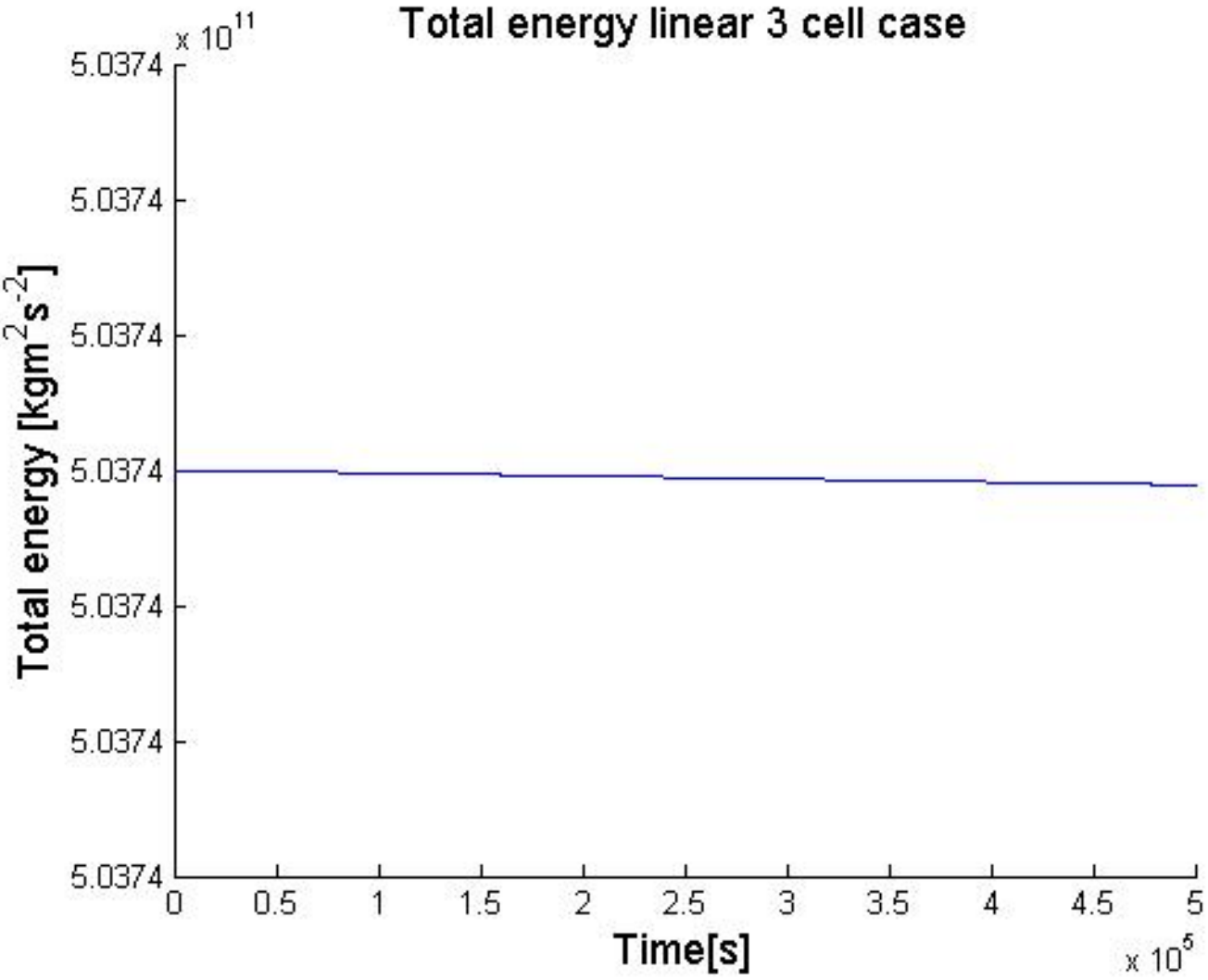

Figure 3.4: Total energy with only $\eta_3 = 1m$ is nonzero initially. Constant depths, 500000s time period.

which are the constant depths angular frequencies. Let us compare the angular frequencies of the variable depths case with the values of the numerical angular frequencies, obtained by the numerical solution of the variable depths case (Fig.3.3). It is hard to accurately measure the smaller period, but the larger one is present in all the solutions, most evidently in the η_3 solution, a simple harmonic oscillation with a 1700s period. This period corresponds to the smaller angular frequency $\frac{\sqrt{g}}{\Delta x}\sqrt{H_1 + H_2 - \sqrt{H_1^2 - H_1H_2 + H_2^2}}$. To end the linear three-cell case discussion, we will show the total energy of the three-cell case as a function of time, utilizing a formula from (Espelid et al., 2000)

$$E_{tot} = E_{kin} + E_{pot} = \frac{1}{2}\rho\Delta x\Delta y \sum_i (H_u U_i^2 + H_v V_i^2 + g\eta_i^2)\,. \tag{3.4}$$

The grid lengths are set to $\Delta x = \Delta y$, since we have chosen a quadratic grid, and the horizontal speeds V_i are zero. H_u and H_v are the depths corresponding to the U_i and V_i velocities positions in the i-th cell. We can see from Fig.3.4 that the energy is almost constant. The time period chosen is longer than normal, 500000s to notice the decrease of energy, likely due to the accumulation of errors. In this chapter, we have calculated eigenvalues and eigenvectors belonging to two different angular frequencies, if we exclude the zero angular frequency. Next chapter, we will study the effect the non-linear term has on the solutions and the eigenvalues of the three-cell case.

Chapter 4

The non-linear three-cell case

In the non-linear three-cell case, we will add the non-linear terms of Eqn.1.2, thus increasing the complexity. We will study what changes with the eigenvalues and the eigenvectors. First we will set up the shallow water equations in the advective form

$$\begin{aligned} \frac{\partial U}{\partial t} + U\frac{\partial U}{\partial x} + V\frac{\partial U}{\partial y} &= -g\frac{\partial \eta}{\partial x}\,, \\ \frac{\partial V}{\partial t} + U\frac{\partial V}{\partial x} + V\frac{\partial V}{\partial y} &= -g\frac{\partial \eta}{\partial y}\,, \end{aligned} \tag{4.1}$$

and then in the flux form

$$\begin{aligned} \frac{\partial U}{\partial t} + \frac{\partial UU}{\partial x} + \frac{\partial UV}{\partial y} &= -g\frac{\partial \eta}{\partial x}\,, \\ \frac{\partial V}{\partial t} + \frac{\partial UV}{\partial x} + \frac{\partial VV}{\partial y} &= -g\frac{\partial \eta}{\partial y}\,. \end{aligned} \tag{4.2}$$

To go from Eqn.4.2 to Eqn.4.1, we apply the product rule on the non-linear terms

$$\begin{aligned} \frac{\partial UU}{\partial x} + \frac{\partial UV}{\partial y} &= U\frac{\partial U}{\partial x} + V\frac{\partial U}{\partial y} + U\frac{\partial U}{\partial x} + U\frac{\partial V}{\partial y}\,, \\ \frac{\partial UV}{\partial x} + \frac{\partial VV}{\partial y} &= U\frac{\partial V}{\partial x} + V\frac{\partial V}{\partial y} + V\frac{\partial U}{\partial x} + V\frac{\partial V}{\partial y}\,. \end{aligned}$$

Since $\nabla \cdot \mathbf{U} = 0$, the two last terms on the right hand side of the equations are equal to zero, and we get

$$\begin{aligned} \frac{\partial UU}{\partial x} + \frac{\partial UV}{\partial y} &= U\frac{\partial U}{\partial x} + V\frac{\partial U}{\partial y}\,, \\ \frac{\partial UV}{\partial x} + \frac{\partial VV}{\partial y} &= U\frac{\partial V}{\partial x} + V\frac{\partial V}{\partial y}\,. \end{aligned}$$

This shows that for an incompressible fluid the two forms Eqn.4.1 and Eqn.4.2 are equivalent. Setting V=0, discretizing Eqn.4.1 and including the surface elevations equations will produce

$$\begin{aligned} \frac{dU_1}{dt} &= -U_1\frac{U_2}{2\Delta x} - g\frac{\eta_2 - \eta_1}{\Delta x}\,, \\ \frac{dU_2}{dt} &= U_2\frac{U_1}{2\Delta x} - g\frac{\eta_3 - \eta_2}{\Delta x}\,, \\ \frac{d\eta_1}{dt} &= -H_1\frac{U_1}{\Delta x}\,, \\ \frac{d\eta_2}{dt} &= H_1\frac{U_1}{\Delta x} - H_2\frac{U_2}{\Delta x}\,, \\ \frac{d\eta_3}{dt} &= H_2\frac{U_2}{\Delta x}\,. \end{aligned} \tag{4.3}$$

By discretizing Eqn.4.2, the ODE's are

$$\begin{aligned}
\frac{dU_1}{dt} &= -\frac{U_2^2}{2\Delta x} - g\frac{\eta_2 - \eta_1}{\Delta x}\,, \\
\frac{dU_2}{dt} &= \frac{U_1^2}{2\Delta x} - g\frac{\eta_3 - \eta_2}{\Delta x}\,, \\
\frac{d\eta_1}{dt} &= -H_1\frac{U_1}{\Delta x}\,, \\
\frac{d\eta_2}{dt} &= H_1\frac{U_1}{\Delta x} - H_2\frac{U_2}{\Delta x}\,, \\
\frac{d\eta_3}{dt} &= H_2\frac{U_2}{\Delta x}\,.
\end{aligned} \tag{4.4}$$

On matrix form, the advective equations are

$$\frac{d}{dt}\mathbf{w}(t) = \begin{pmatrix}
-\frac{U_2}{2\Delta x} & 0 & \frac{g}{\Delta x} & -\frac{g}{\Delta x} & 0 \\
0 & \frac{U_1}{2\Delta x} & 0 & \frac{g}{\Delta x} & -\frac{g}{\Delta x} \\
-\frac{H_1}{\Delta x} & 0 & 0 & 0 & 0 \\
\frac{H_1}{\Delta x} & -\frac{H_2}{\Delta x} & 0 & 0 & 0 \\
0 & \frac{H_2}{\Delta x} & 0 & 0 & 0
\end{pmatrix}\mathbf{w}(t)\,,$$

and the flux form equations are

$$\frac{d}{dt}\mathbf{w}(t) = \begin{pmatrix}
0 & -\frac{U_2}{2\Delta x} & \frac{g}{\Delta x} & -\frac{g}{\Delta x} & 0 \\
\frac{U_1}{2\Delta x} & 0 & 0 & \frac{g}{\Delta x} & -\frac{g}{\Delta x} \\
-\frac{H_1}{\Delta x} & 0 & 0 & 0 & 0 \\
\frac{H_1}{\Delta x} & -\frac{H_2}{\Delta x} & 0 & 0 & 0 \\
0 & \frac{H_2}{\Delta x} & 0 & 0 & 0
\end{pmatrix}\mathbf{w}(t)\,.$$

The numerical solutions for the non-linear equations, using the advective form, give approximately the same results as the linear case in Fig.3.2. However, in Fig.4.1, we are shown the differences between the non-linear and linear three-cell case, which amount to $O(10^{-3})$. The standard initial values have been used, only $\eta_3 = 1m$ is non-zero initially. The non-linear and linear solutions differences are oscillating functions where the amplitude oscillates as well. These functions form envelopes, an envelope contains two angular frequencies. The shorter oscillations have periods of about 1200s, and the larger oscillations have periods of approximately 15000s. Shown in Fig.4.2 are the differences of the flux and advective form. They are miniscule as well, and oscillate on the order $O(10^{-3})$. Only the difference of the η_2 solutions has a constant angular frequency. The other differences of solutions in Fig.4.2 are envelopes, consisting of two different angular frequencies. The large oscillations of the envelopes have periods of about 15000s and the smaller oscillations have periods of 2500s. In (Kundu and Cohen, 2008) the wave packet is defined as half the size of the period, L, which is inversely proportional to the bandwidth $L \propto \frac{1}{\Delta k}$. Δk is the bandwidth size of the wave number. We consider all the envelopes in Fig.4.2 and Fig.4.1 as wave packets. The two figures contain two different envelopes, with the same bandwidth, centered at two different wave numbers. The non-linear solutions phase shift the linear solutions forwards a small amount, then backwards to the initial positions at 7500s, before it begins shifting again. For the change to flux to advective form, we have the same kind of phase shifts as well. The solution is shifted forwards and backwards to the initial values in 7500s. The exception is the difference of the η_2 solutions in Fig.4.2, which seems to taper the peaks and trough of the solution.

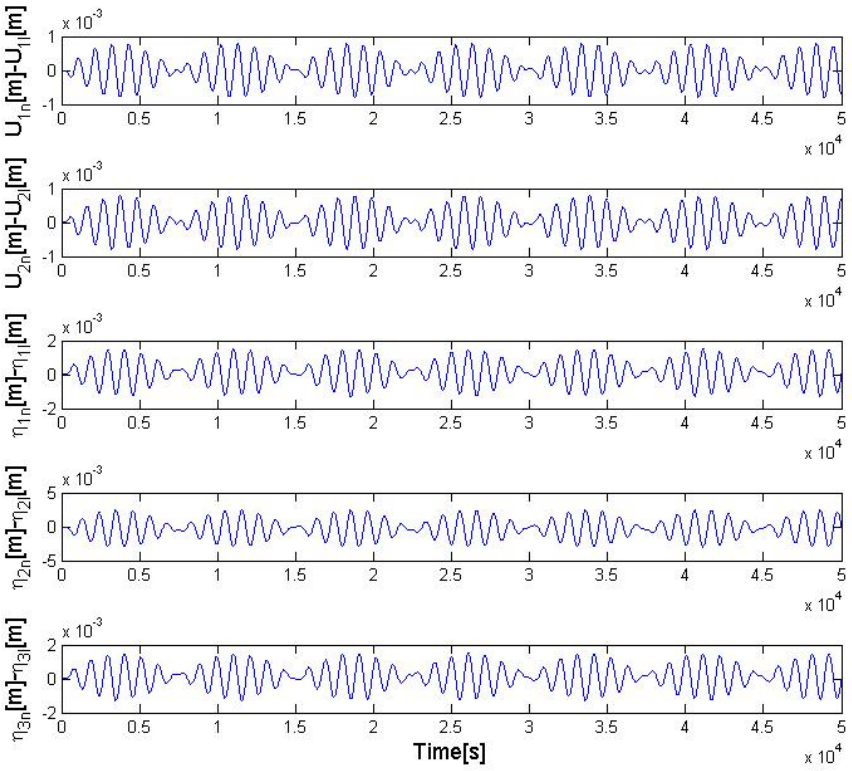

Figure 4.1: The difference between linear and non-linear case. The time period is set to 50000s, to make the envelopes observable.

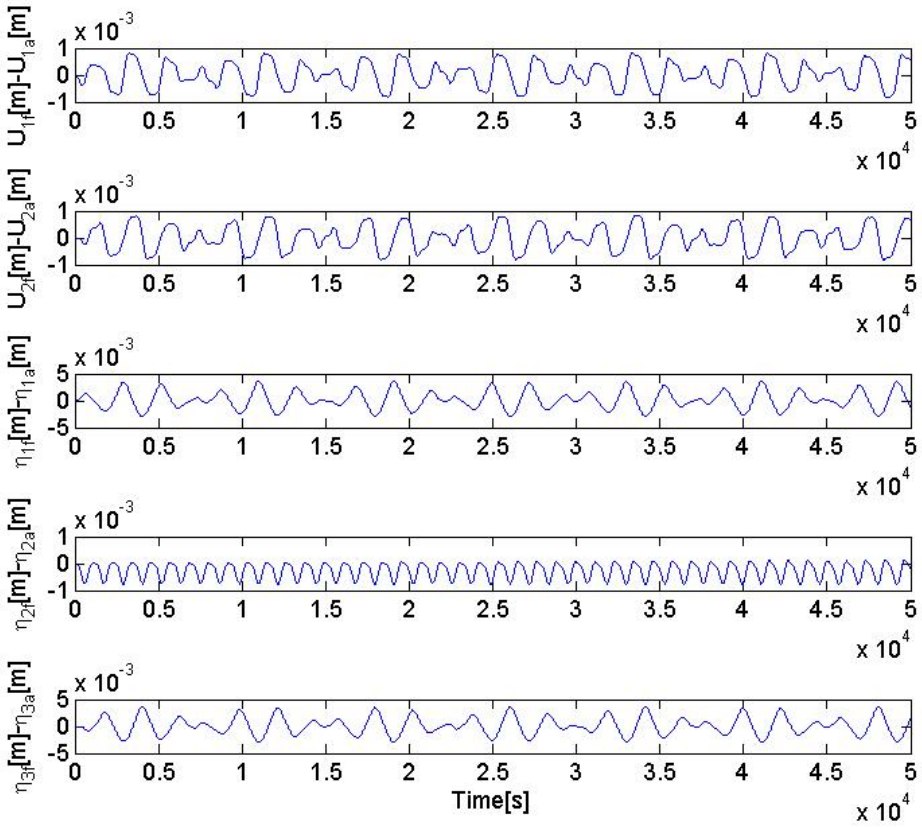

Figure 4.2: The difference of the flux and advective form. The time period is 50000s.

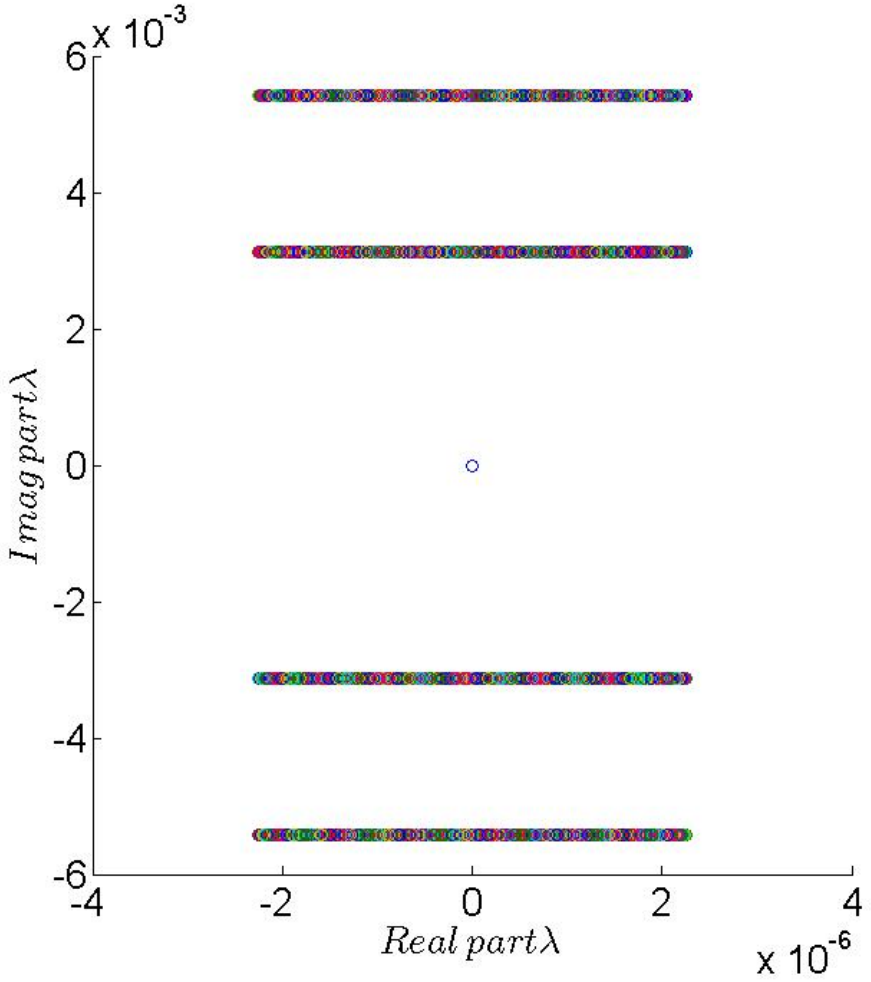

Figure 4.3: The eigenvalues of the advective form. The flux form eigenvalues are basically the same, but with some subtle differences. Each circle represents an eigenvalue. We have λ_3 and λ_1 on top of the figure, λ_0 in the middle at the origin, and on the bottom of the figure, λ_2 and λ_4 . Expanded view of the λ_3 and the λ_1 eigenvalues are shown in Fig.4.8 and Fig.4.9.

Applying the flux form produces almost the same eigenvalues as the advective form and the eigenvalues appear to be constrained in the same ranges, as shown in Fig.4.3. The eigenvalues depend on the velocities at a given time in the non-linear case. The discretization method used, the trapezoidal scheme, seems to average out this potential instability. We have an error in the real part of $O(10^{-6})$, but it is confined in that range, likewise with the imaginary part, which is of $O(10^{-9})$.

Shown in Fig.4.4 and Fig.4.5 are the real and imaginary values of λ_3. The solutions are oscillating, the amplitude is constant for the real part and the imaginary part is forming envelopes. We have a similar situation for λ_1, as shown in Fig.4.6 and Fig.4.7. The real part is the same in both forms, not out of phase with each other and the amplitude of the envelope for the imaginary part is slightly stronger. Lines have been drawn instead of circles in these figures to make them easier to read. We have 500 eigenvalues in each, the amount of eigenvalues are large enough to replace it with a continuous function without noticing. The figures tell us the eigenvalues are constrained.

Shown in Fig. 4.8 is the phase portrait of the eigenvalues of the advective form matrix and in Fig.4.9 we have shown the phase portrait of the flux form matrix. We can see that the eigenvalues appear to be constrained in boxed areas oscillating between fixed values. The time period for these eigenvalues are 50000s to make the lines more pronounced. The energy for both the advective and flux form, shown in Fig.4.10, is not constant in contrast with the linear case (Fig.3.4). Closing this chapter, we have seen that the numerical solution of the non-linear three-cell case contained some stable properties. Despite the flux and advective form propagation matrices were not similar to skew-symmetric matrices. In the next chapter, we will find a form that has constant energy for the non-linear constant depths case.

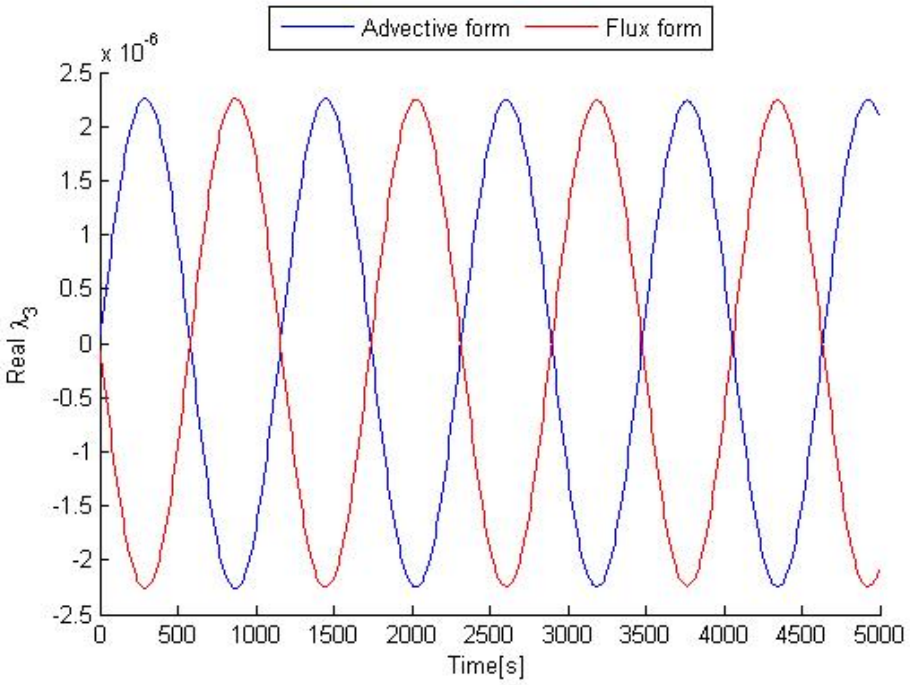

Figure 4.4: The real part of λ_3 of the propagation matrix, advective and flux form.

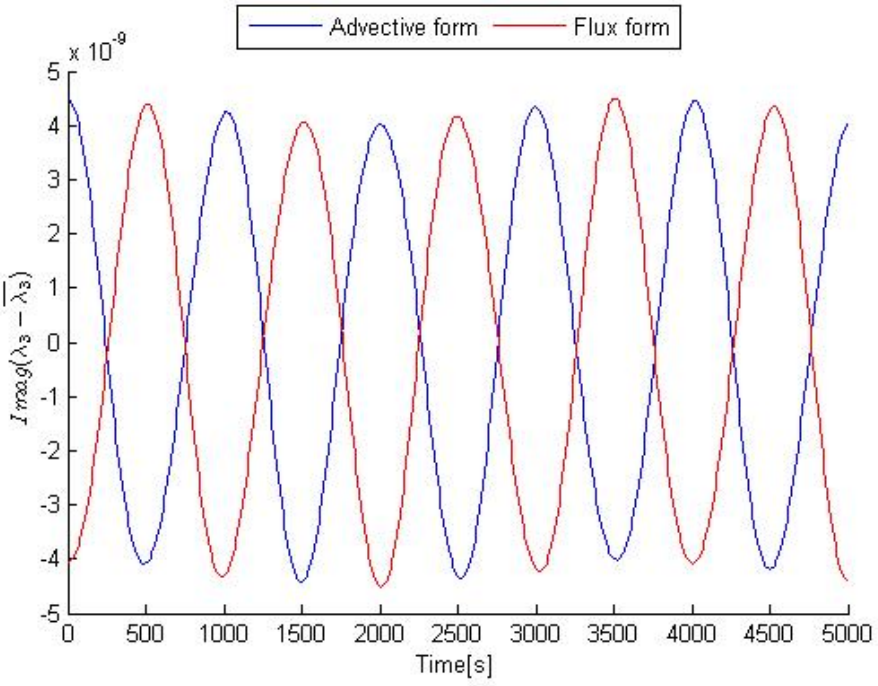

Figure 4.5: The imaginary part of λ_3 of the propagation matrix, advective and flux form. The mean value is subtracted. $\overline{\lambda}_3$ means average value in this figure.

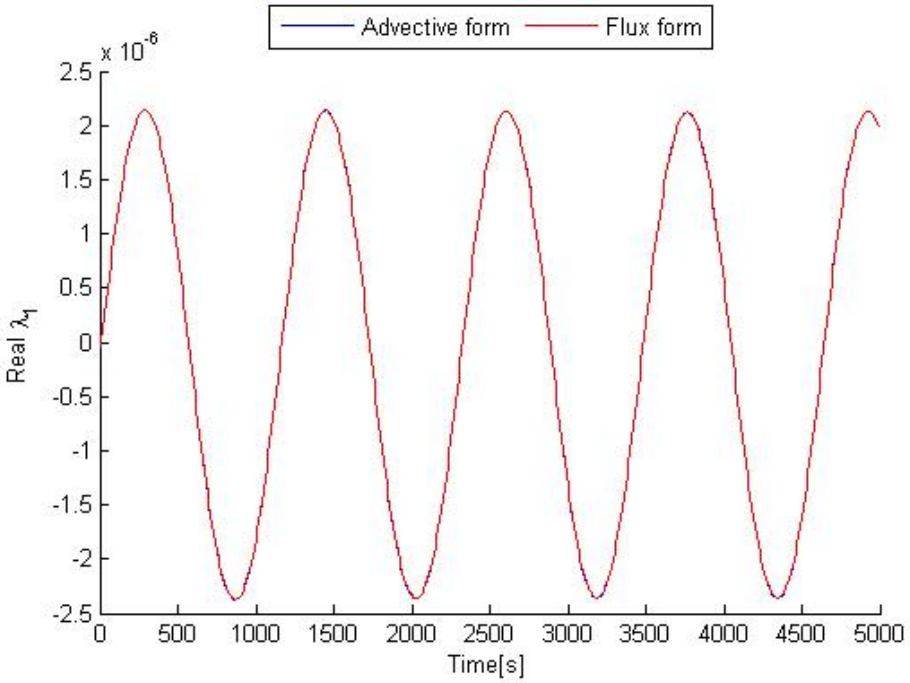

Figure 4.6: The real part of λ_1 of the propagation matrix, advective and flux form. The solutions are overlapping.

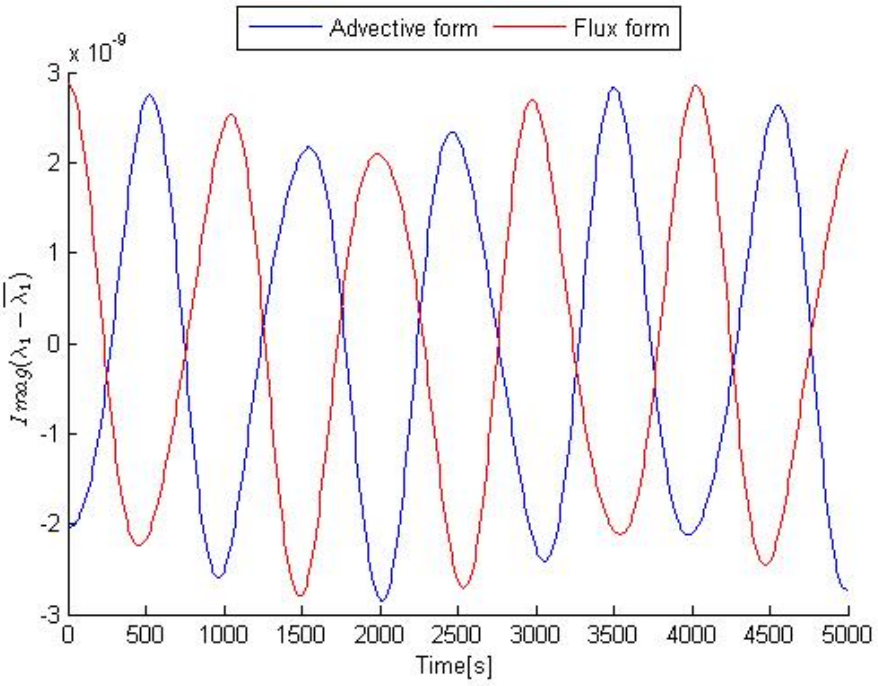

Figure 4.7: The imaginary part of λ_1 of the advective and flux form propagation matrix, mean value subtracted. $\overline{\lambda}_1$ means average value in this figure.

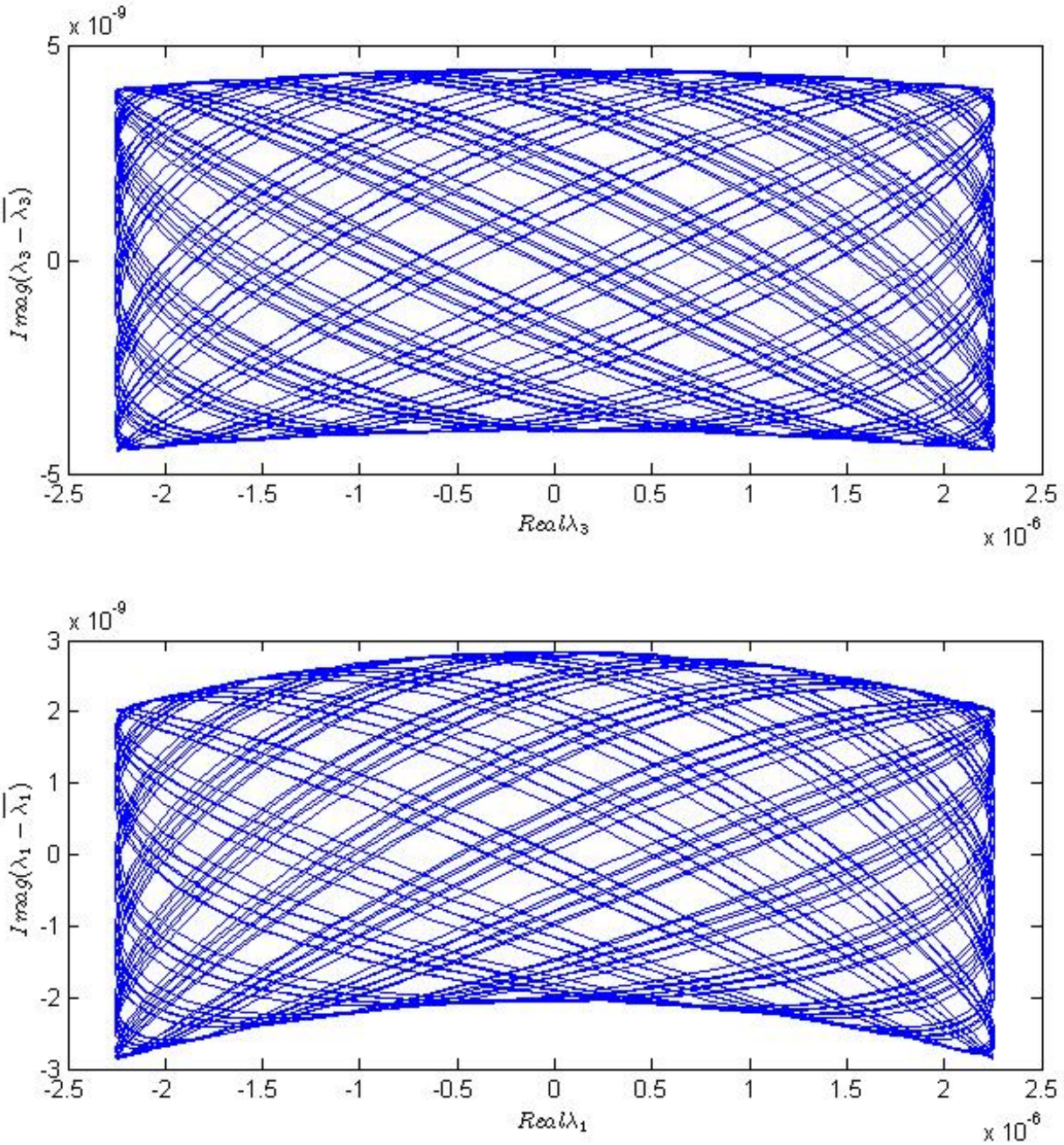

Figure 4.8: Phase portraits of the λ_1 and the λ_3 eigenvalues of the advective form matrix over 50000s. Imaginary mean subtracted, $\overline{\lambda}_1$ and $\overline{\lambda}_3$ means average value in these figures.

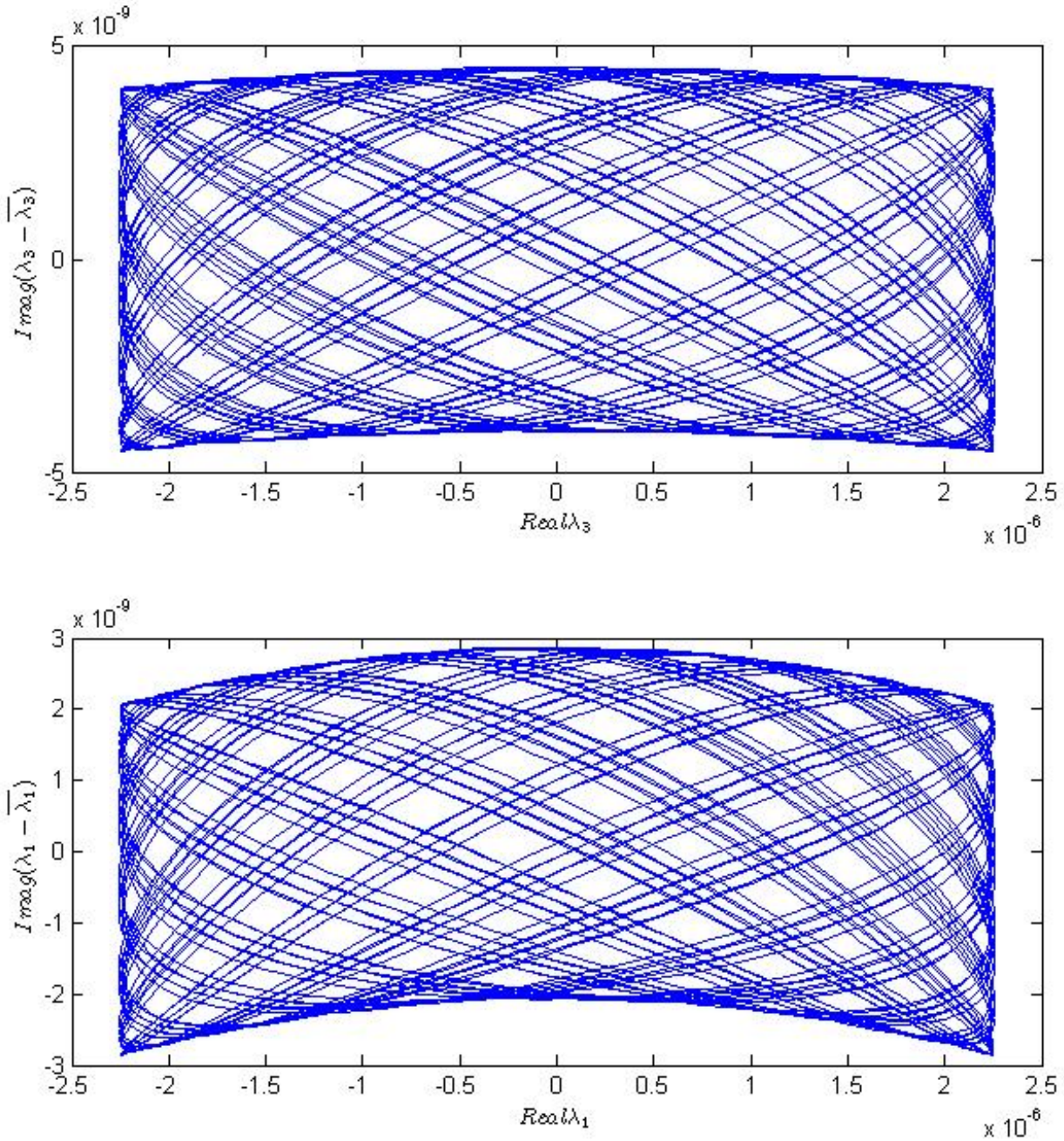

Figure 4.9: Phase portraits of the λ_1 and the λ_3 eigenvalues of the flux form matrix. The time period is 50000s, imaginary mean subtracted, $\overline{\lambda}_1$ and $\overline{\lambda}_3$ means average value in these figures.

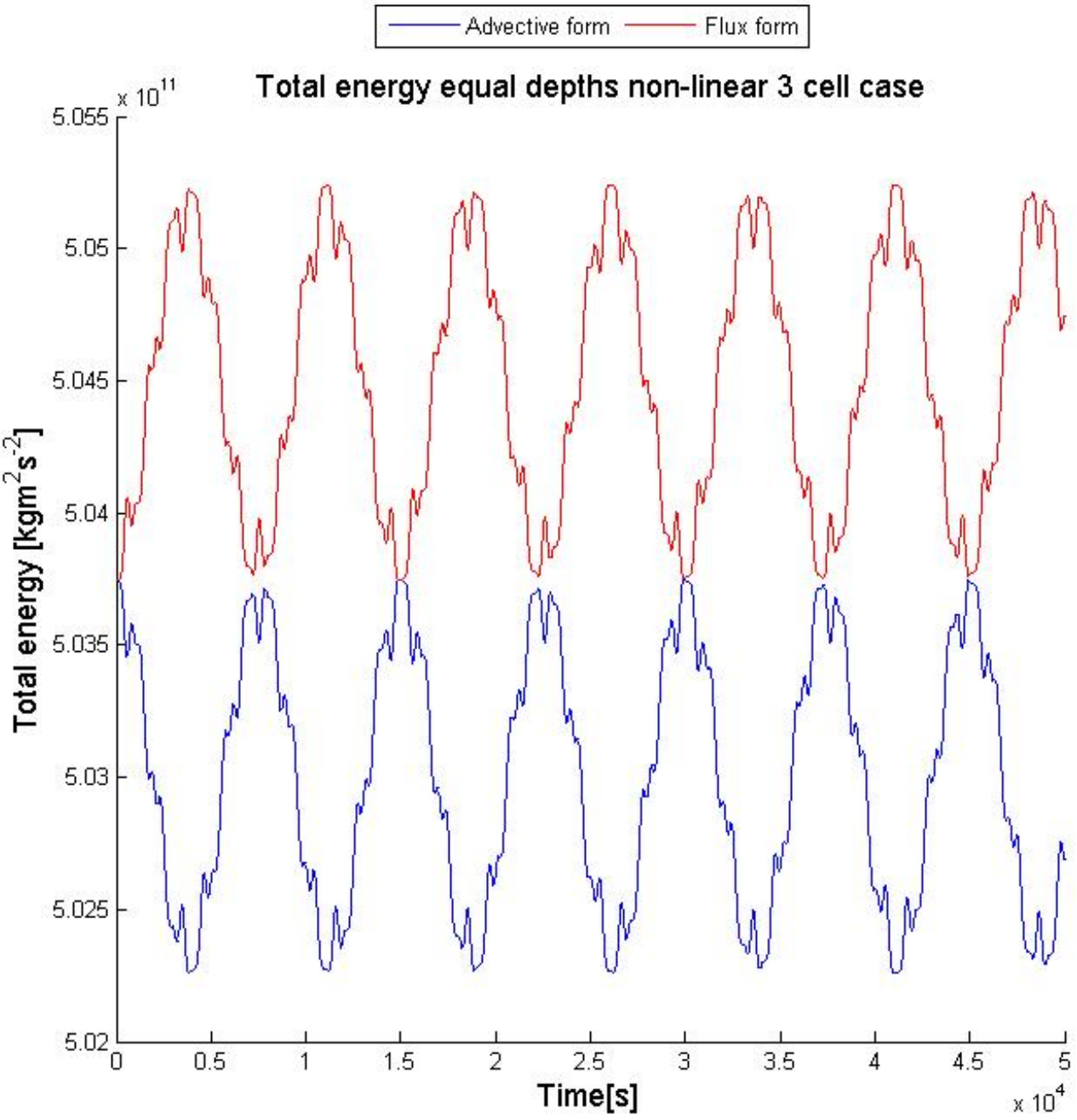

Figure 4.10: Total energy for the advective and flux form.

Chapter 5

The non-linear three-cell case: skew-symmetric form

The amplitude error in the solution of the three-cell case will increase if the size of non-zero real part increases, so we wish to reduce that part as much as possible. We will reduce the real parts of the eigenvalues by changing the discretization. Any linear combination of the two forms Eqn.4.4 and Eqn.4.3 can be used to form a new discretization. In particular, the average between the two forms gives a promising set of equations, the result is shown in Eqn.5.1. We get to this set of equations by taking the average of the non-linear term in the flux and the advective form

$$-\frac{U_2^2}{4\Delta x} - U_1\frac{U_2}{4\Delta x} = -\frac{U_2(U_1+U_2)}{4\Delta x}\,,$$

$$\frac{U_1^2}{4\Delta x} + U_1\frac{U_2}{4\Delta x} = \frac{U_1(U_1+U_2)}{4\Delta x}\,.$$

These non-linear parts inserted into the total set of equations becomes

$$\begin{aligned}
\frac{dU_1}{dt} &= -\frac{U_2(U_1+U_2)}{4\Delta x} - g\frac{\eta_2-\eta_1}{\Delta x}\,,\\
\frac{dU_2}{dt} &= \frac{U_1(U_1+U_2)}{4\Delta x} - g\frac{\eta_3-\eta_2}{\Delta x}\,,\\
\frac{d\eta_1}{dt} &= -H_1\frac{U_1}{\Delta x}\,,\\
\frac{d\eta_2}{dt} &= H_1\frac{U_1}{\Delta x} - H_2\frac{U_2}{\Delta x}\,,\\
\frac{d\eta_3}{dt} &= H_2\frac{U_2}{\Delta x}\,.
\end{aligned} \tag{5.1}$$

Eqn.5.1 gives a sign skew-symmetric matrix A in matrix form

$$\frac{d}{dt}\mathbf{w}(t) = \begin{pmatrix}
0 & -\frac{(U_2+U_1)}{4\Delta x} & \frac{g}{\Delta x} & -\frac{g}{\Delta x} & 0\\
\frac{(U_1+U_2)}{4\Delta x} & 0 & 0 & \frac{g}{\Delta x} & -\frac{g}{\Delta x}\\
-\frac{H_1}{\Delta x} & 0 & 0 & 0 & 0\\
\frac{H_1}{\Delta x} & -\frac{H_2}{\Delta x} & 0 & 0 & 0\\
0 & \frac{H_2}{\Delta x} & 0 & 0 & 0
\end{pmatrix}\mathbf{w}(t) = A\mathbf{w}(t)\,.$$

The matrix A is similar to a skew-symmetric matrix when $H_1 = H_2$, by the change of basis $D^{-1}AD$, where

$$D = \begin{pmatrix} \sqrt{\frac{g}{H_1}} & 0 & 0 & 0 & 0 \\ 0 & \sqrt{\frac{g}{H_2}} & 0 & 0 & 0 \\ 0 & 0 & 1 & 0 & 0 \\ 0 & 0 & 0 & 1 & 0 \\ 0 & 0 & 0 & 0 & 1 \end{pmatrix}.$$

We split A into two parts, to effectively find a skew-symmetric form, $A = \tilde{A} + B$, where

$$\tilde{A} = \begin{pmatrix} 0 & -\frac{(U_1+U_2)}{4\Delta x} & 0 & 0 & 0 \\ \frac{(U_1+U_2)}{4\Delta x} & 0 & 0 & 0 & 0 \\ 0 & 0 & 0 & 0 & 0 \\ 0 & 0 & 0 & 0 & 0 \\ 0 & 0 & 0 & 0 & 0 \end{pmatrix},$$

$$B = \begin{pmatrix} 0 & 0 & \frac{g}{\Delta x} & -\frac{g}{\Delta x} & 0 \\ 0 & 0 & 0 & \frac{g}{\Delta x} & -\frac{g}{\Delta x} \\ -\frac{H_1}{\Delta x} & 0 & 0 & 0 & 0 \\ \frac{H_1}{\Delta x} & -\frac{H_2}{\Delta x} & 0 & 0 & 0 \\ 0 & \frac{H_2}{\Delta x} & 0 & 0 & 0 \end{pmatrix}.$$

Taking the similarity transform of A, we get $D^{-1}AD = D^{-1}\tilde{A}D + D^{-1}BD$. In this expression, $D^{-1}BD$ is skew-symmetric, while $D^{-1}\tilde{A}D$ is not, when $H_1 = H_2$

$$D^{-1}\tilde{A}D = \begin{pmatrix} 0 & -\frac{(U_1+U_2)}{4\Delta x}\sqrt{\frac{H_2}{H_1}} & 0 & 0 & 0 \\ \frac{(U_1+U_2)}{4\Delta x}\sqrt{\frac{H_1}{H_2}} & 0 & 0 & 0 & 0 \\ 0 & 0 & 0 & 0 & 0 \\ 0 & 0 & 0 & 0 & 0 \\ 0 & 0 & 0 & 0 & 0 \end{pmatrix}.$$

We turn now to the numerical solution of the constant depths case using the propagation matrix A with the standard initial values, the same as we used in the linear case. The eigenvalues given in Fig.5.1, show that the magnitude of the real parts of the eigenvalues are significantly lower than in the previous dicretizations, of $O(10^{-18})$, which is of machine level precision. This is an improvement for the stability for the given initial values. The total energy is approximately constant as it was for the linear case, as portrayed in Fig.5.2 . For the variable depths case however, this method does not reduce the real part as

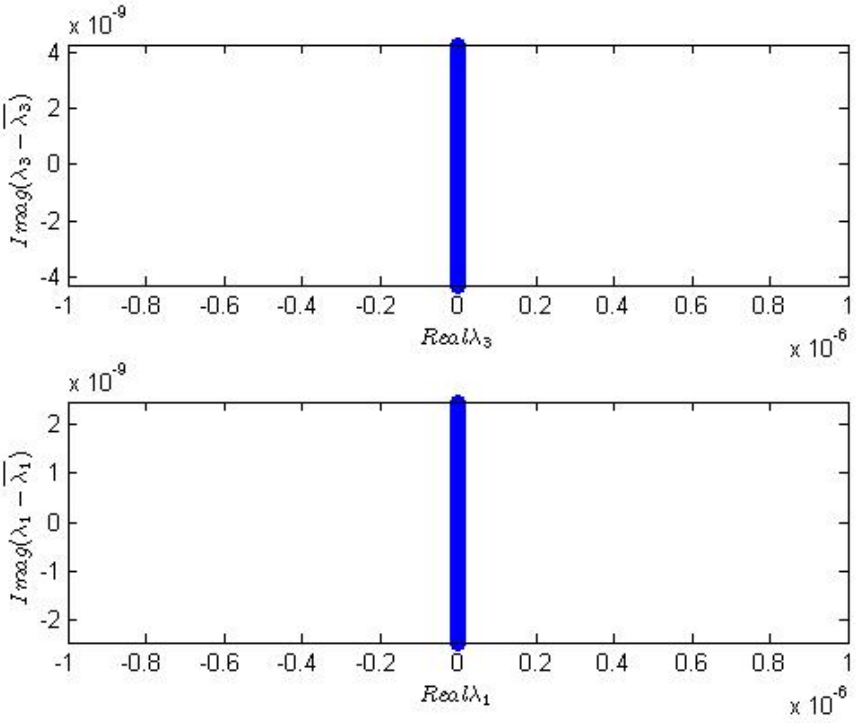

Figure 5.1: The eigenvalue distribution of the skew-symmetric form, mean imaginary value subtracted, constant depths. $\overline{\lambda}_1$ and $\overline{\lambda}_3$ means average value in these figures. $\eta_3 = 1m$ initially.

desired. In Fig.5.3 we see the that the eigenvalues gain a noticeable real part, only with a small difference in the depths $\Delta H = 3m$. The propagation matrix A is not similar to a skew-symmetric matrix if $H_1 \neq H_2$, but we can amend this by weighting the part $\tilde{A}$ of A with the square root depths ratio produced in the similarity transformation. Furthermore, we can replace A with $C = D^{-1}\tilde{A}D + B$ as the propagation matrix to obtain

$$\frac{d}{dt}\mathbf{w}(t) = \begin{pmatrix} 0 & -\frac{(U_2+U_1)}{4\Delta x}\sqrt{\frac{H_2}{H_1}} & \frac{g}{\Delta x} & -\frac{g}{\Delta x} & 0 \\ \frac{(U_1+U_2)}{4\Delta x}\sqrt{\frac{H_1}{H_2}} & 0 & 0 & \frac{g}{\Delta x} & -\frac{g}{\Delta x} \\ -\frac{H_1}{\Delta x} & 0 & 0 & 0 & 0 \\ \frac{H_1}{\Delta x} & -\frac{H_2}{\Delta x} & 0 & 0 & 0 \\ 0 & \frac{H_2}{\Delta x} & 0 & 0 & 0 \end{pmatrix} \mathbf{w}(t) = C\mathbf{w}(t)\,.$$

Instead of large real parts, the eigenvalues in this propagation matrix have large errors in the imaginary part, but these errors are less when $H_1 >> H_2$ or $H_2 >> H_1$. From a theoretical standpoint, this method is weak. Instead one could use upstream schemes, but determining stability is not easily done as the corresponding propagation matrix is changing signs in the entries, potentially at each time step. The skew-symmetric form we found in this chapter for constant depths gives similar propagation matrices for the four-, five- and n-cell cases. Adding the advective and flux form gives a skew-symmetric form for constant depths for all of the n-cell cases. However, in the next chapter we will use a different tessellation than in the previous two- and three-cell cases. In the four-cell case we will form a square, which gives a different propagation matrix.

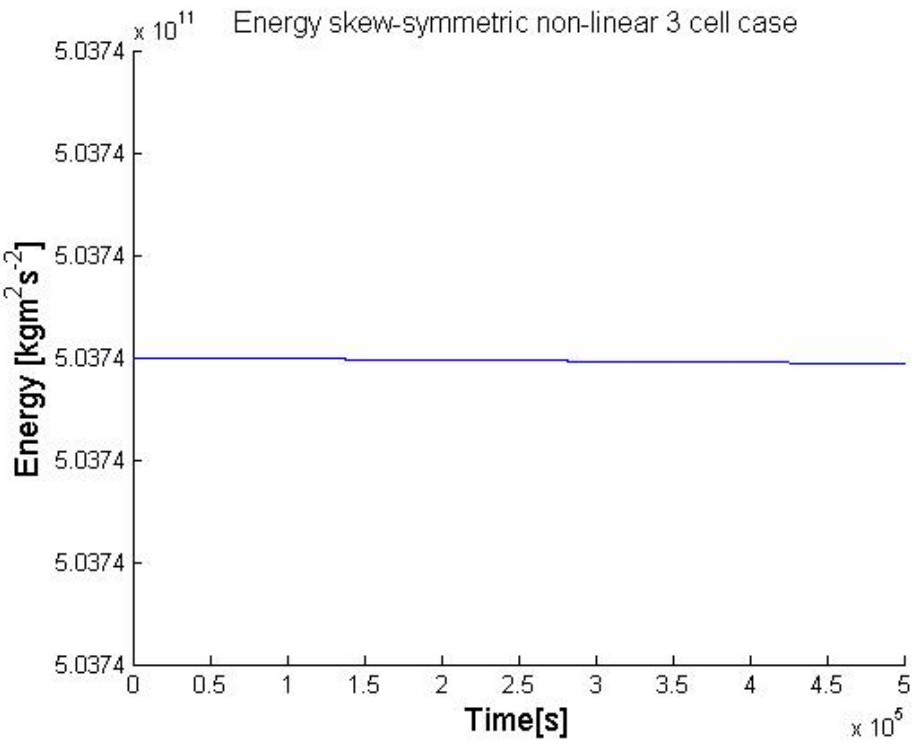

Figure 5.2: Energy of the skew-symmetric form, $\eta_3 = 1m$ initially.

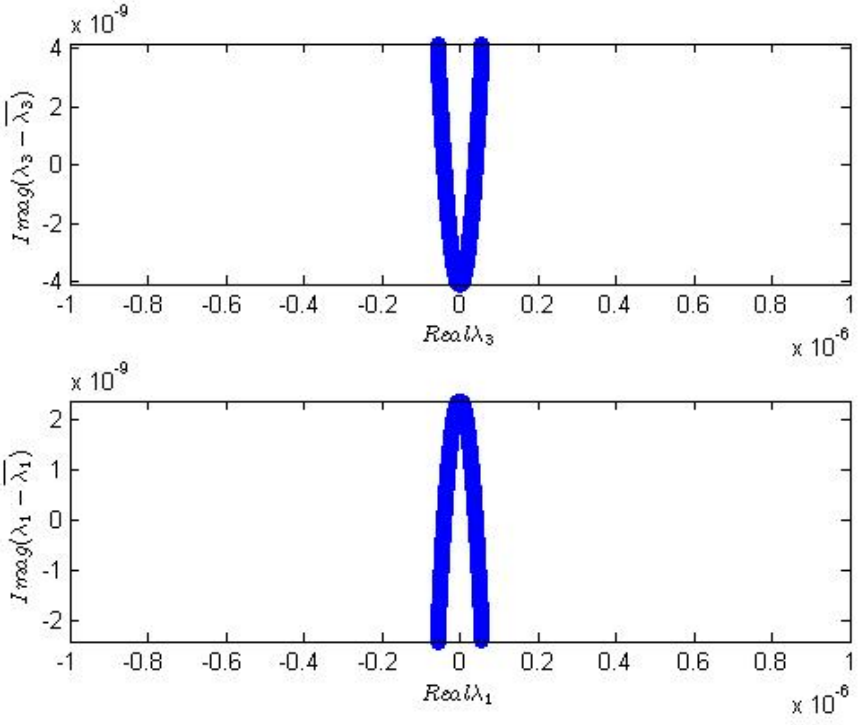

Figure 5.3: The eigenvalue distribution of the skew-symmetric form, $H_1 = 100m$, $H_2 = 103m$. $\overline{\lambda}_1$ and $\overline{\lambda}_3$ means average value in these figures. $\eta_3 = 1m$ initially.

Chapter 6

The linear four-cell case

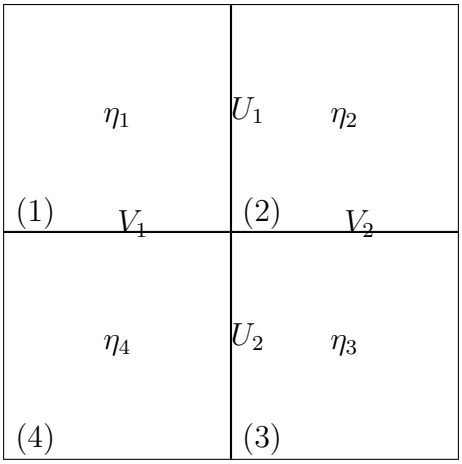

Figure 6.1: Variables of the four-cell case. The cells are numbered 1 to 4.

By using a square ordering of the grid cells in the four-cell case, we introduce the y-variable depth-averaged velocities, surface elevations and depths. In the four-cell case we have the 8 variables shown in Fig.6.1. The cells are numbered 1 to 4 in a clockwise direction. In addition, we have four depths H_1,H_2,H_3 and H_4, positioned corresponding to the velocities U_1,V_2,U_2 and V_1 positions. The grid distance is Δx in the x-direction and Δy in the y-direction. We will use quadratic grids for the four-cell case, as we did for the two-cell and the three-cell case, so we set $\Delta x = \Delta y$. The discretized shallow water equations for the four-cell case are written

$$\begin{aligned}
\frac{dU_1}{dt} &= -g\frac{\eta_2-\eta_1}{\Delta x}\,,\\
\frac{dU_2}{dt} &= -g\frac{\eta_3-\eta_4}{\Delta x}\,,\\
\frac{dV_1}{dt} &= -g\frac{\eta_1-\eta_4}{\Delta y}\,,\\
\frac{dV_2}{dt} &= -g\frac{\eta_2-\eta_3}{\Delta y}\,,\\
\frac{d\eta_1}{dt} &= -H_1\frac{U_1}{\Delta x}+H_4\frac{V_1}{\Delta y}\,,\\
\frac{d\eta_2}{dt} &= H_1\frac{U_1}{\Delta x}+H_2\frac{V_2}{\Delta y}\,,\\
\frac{d\eta_3}{dt} &= H_3\frac{U_2}{\Delta x}-H_2\frac{V_2}{\Delta y}\,,\\
\frac{d\eta_4}{dt} &= -H_3\frac{U_2}{\Delta x}-H_4\frac{V_1}{\Delta y}\,.
\end{aligned} \tag{6.1}$$

The system of the ODE's is summed up in a 8 by 8 propagation matrix

$$\frac{d}{dt}\mathbf{w}(t) = A\mathbf{w}(t)\,,$$

$$\frac{d}{dt}\mathbf{w}(t) = \begin{pmatrix} 0 & 0 & 0 & 0 & \frac{g}{\Delta x} & -\frac{g}{\Delta x} & 0 & 0 \\ 0 & 0 & 0 & 0 & 0 & 0 & -\frac{g}{\Delta x} & \frac{g}{\Delta x} \\ 0 & 0 & 0 & 0 & -\frac{g}{\Delta y} & 0 & 0 & \frac{g}{\Delta y} \\ 0 & 0 & 0 & 0 & 0 & -\frac{g}{\Delta y} & \frac{g}{\Delta y} & 0 \\ -\frac{H_1}{\Delta x} & 0 & \frac{H_4}{\Delta y} & 0 & 0 & 0 & 0 & 0 \\ \frac{H_1}{\Delta x} & 0 & 0 & \frac{H_2}{\Delta y} & 0 & 0 & 0 & 0 \\ 0 & \frac{H_3}{\Delta x} & 0 & -\frac{H_2}{\Delta y} & 0 & 0 & 0 & 0 \\ 0 & -\frac{H_3}{\Delta x} & -\frac{H_4}{\Delta y} & 0 & 0 & 0 & 0 & 0 \end{pmatrix} \begin{pmatrix} U_1(t) \\ U_2(t) \\ V_1(t) \\ V_2(t) \\ \eta_1(t) \\ \eta_2(t) \\ \eta_3(t) \\ \eta_4(t) \end{pmatrix}.$$

It is not easy to get the simple exact solutions for the eigenvalues, as the characteristic equation for the propagation matrix is only reducible to a degree of four, which in turn gives long expressions of the eigenvalues. We will instead evaluate the eigenvalues numerically. All the eigenvalues in this chapter have a $O(10^{-18})$ real part. There will be four pairs of eigenvalues and eigenvectors, if we include the zero eigenvalues and eigenvectors. This means a possibility of three different angular frequencies in the solutions. The eigenvalues will be numbered as follows: λ_0 and λ_1, the zero value eigenvalues; λ_2 and λ_3, complex conjugates of the second non-zero eigenvalue; λ_4 and λ_5, complex conjugates of the first non-zero eigenvalue; λ_6 and λ_7, complex conjugates of the third non-zero eigenvalue. The eigenvectors indexes will correspond to the eigenvalue indices. Shown in Fig.6.2 is the numerical solution of Eqn.6.1, when we put $\Delta x = \Delta y = 10000m$, H_1,H_2,H_3, $H_4 = 100m$ and

$$\mathbf{w}(0) = \begin{pmatrix} 0 \\ 0 \\ 0 \\ 0 \\ 0 \\ 0 \\ 0 \\ 1 \end{pmatrix}.$$

The periods of the oscillations are in general smaller than the periods in the two-cell case (Fig.2.2), and the three-cell case (Fig.3.2). The shortest period in the constant depths four-cell case is about 1000s long, exemplified by the η_3 solution. The four-cell case can spread out faster than the three-cell case, since we have multiple directions for the water to spread to. Moreover, we observe that the η_3 and η_1 solutions are identical to each other, and this show the symmetry of the model.

Furthermore, the U_1 and V_2 solutions are equal, since the water leaving cell 4 is equally distributed in both the x- and y-direction. All this shows that we have a pure diagonal mode with these initial values. Other modes will be produced if we set the initial surface elevation equal in the x-direction or y-direction. The following two initial values render the same motion as the two-cell case

$$\mathbf{w}(0) = \begin{pmatrix} 0 \\ 0 \\ 0 \\ 0 \\ 0 \\ 0 \\ 1 \\ 1 \end{pmatrix}, \; \mathbf{w}(0) = \begin{pmatrix} 0 \\ 0 \\ 0 \\ 0 \\ 1 \\ 1 \\ 0 \\ 0 \end{pmatrix}.$$

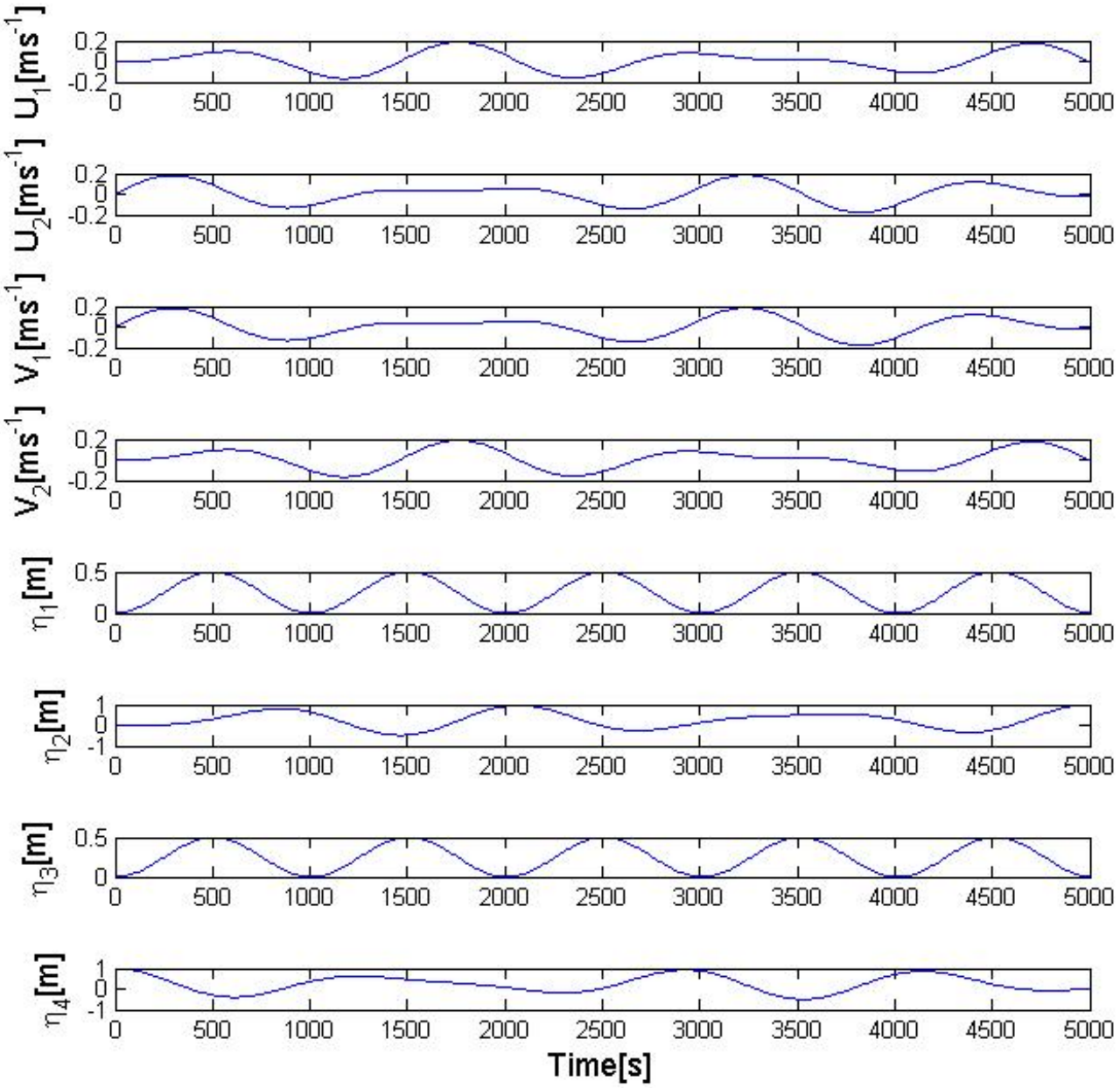

Figure 6.2: The four-cell case solution. With constant depths, $H_1, H_2, H_3, H_4 = 100m$. Initial surface elevation is 1m at η_4, and the rest of the initial values are 0.

If $\Delta x \neq \Delta y$ then these two initial values will give different periods, since they will belong to two different sized cells. In Fig.6.3, various modes are shown, obtained in the linear four-cell case. The arrows indicate the direction the velocities have between the cells. We have a mode that is a circular flow (Mode 1), a mode that moves from one corner to another corner diagonally (Mode 2), a mode that moves from left to right in both the upper and lower part of the whole cell (Mode 3) and a mode which the velocities change direction from the upper to the lower part of the whole cell (Mode 4). All of these modes can be reversed direction on, by replacing each surface elevation with its negative. The figures of modes we will show next, will have the values of the surface elevations at the time t=0.

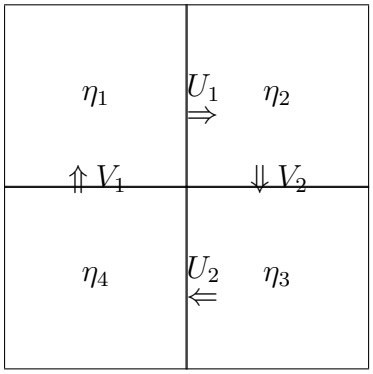

$a) Mode\,1$

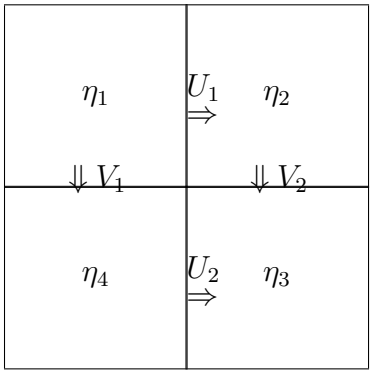

$b) Mode\,2$

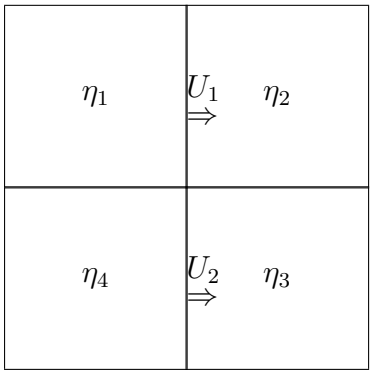

$c) Mode\,3$

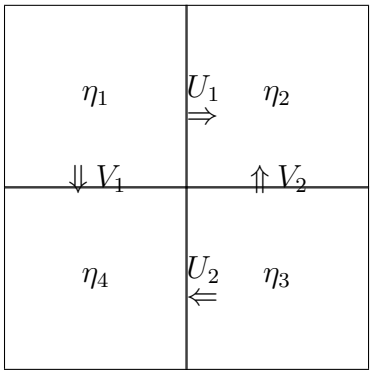

$d) Mode\,4$

Figure 6.3: Sketch of four independent modes of the linear four-cell case with velocities' directions.

The zero eigenvalue and the smallest eigenvalue have multiple eigenvectors that are not complex conjugates of each other. We will now show the eigenvectors corresponding to the positive imaginary eigenvalues

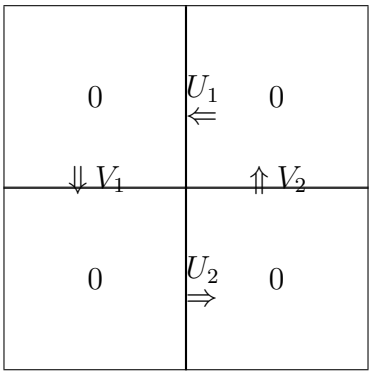

$a) Mode\,1$

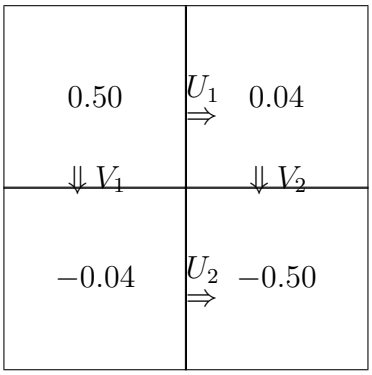

$b) Mode\,2$

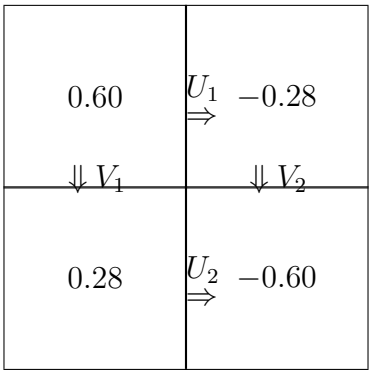

$c) Mode\,3$

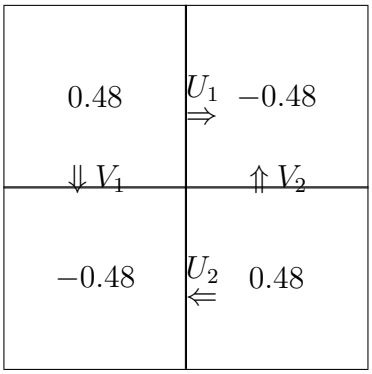

$d) Mode\,4$

Figure 6.4: The modes of constant depths case $H_1, H_2, H_3, H_4 = 100m$ with the velocities directions. The values in the cells are initial surface elevation, the arrows indicate the instantaneous flow direction.

$\lambda_0 = 0, \lambda_1 = 0, \lambda_2 = 0.0044i, \lambda_4 = 0.0044i, \lambda_6 = 0.0063i,$

$$\mathbf{x}_0 = \begin{pmatrix} -0.50 \\ 0.50 \\ -0.50 \\ 0.50 \\ 0 \\ 0 \\ 0 \\ 0 \end{pmatrix}, \mathbf{x}_1 = \begin{pmatrix} -0.10 \\ 0.10 \\ -0.10 \\ 0.10 \\ -0.49 \\ -0.49 \\ -0.49 \\ -0.49 \end{pmatrix}, \mathbf{x}_2 = \begin{pmatrix} -0.10 - 0.10i \\ -0.10 - 0.10i \\ -0.10 + 0.12i \\ -0.10 + 0.12i \\ 0.50 \\ 0.04 + 0.46i \\ -0.50 \\ -0.04 - 0.46i \end{pmatrix},$$

$$\mathbf{x}_4 = \begin{pmatrix} 0.03 - 0.19i \\ 0.03 - 0.19i \\ 0.03 + 0.07i \\ 0.03 + 0.07i \\ 0.60 \\ -0.28 - 0.15i \\ -0.60 \\ 0.28 + 0.15i \end{pmatrix}, \mathbf{x}_6 = \begin{pmatrix} -0.15i \\ 0.15i \\ 0.15i \\ -0.15i \\ 0.48 \\ -0.48 \\ 0.48 \\ -0.48 \end{pmatrix}.$$

The eigenvalues and eigenvectors are used in the solution of Eqn.6.1, written on the form

$$\mathbf{w}(t) = \sum_{i=0}^{7} d_i \mathbf{x}_i e^{\lambda_i t} \,. \tag{6.2}$$

The coefficient d_i is a constant. We will now demonstrate how to read the eigenvalues and vectors to construct a general solution. From a linear combination of the $\mathbf{x}_i$ and $\overline{\mathbf{x}}_i$ eigenvalues as initial values, we get by applying the principle of superposition of solutions for linear ODE's

$$\begin{aligned}
\mathbf{w}(t) = M\mathbf{x}_i e^{\lambda_i t} + N\overline{\mathbf{x}}_i e^{\overline{\lambda}_i t} = \\
M\mathbf{x}_i(\cos|\lambda_i t| + i\sin|\lambda_i t|) + N\overline{\mathbf{x}}_i(\cos|\lambda_i t| - i\sin|\lambda_i t|) = \\
MReal(\mathbf{x}_i)(\cos|\lambda_i t| + i\sin|\lambda_i t|) + MImag(\mathbf{x}_i)i(\cos|\lambda_i t| + i\sin|\lambda_i t|) + \\
NReal(\overline{\mathbf{x}}_i)(\cos|\lambda|_i t - i\sin|\lambda_i t|) + NImag(\overline{\mathbf{x}}_i)i(\cos|\lambda_i t| - i\sin|\lambda_i t|) = \\
(M+N)Real(\mathbf{x}_i)\cos|\lambda_i t| + (M-N)Real(\mathbf{x}_i)i\sin|\lambda_i t| + \\
(M-N)Imag(\mathbf{x}_i)i\cos|\lambda_i t| - (M+N)Imag(\mathbf{x}_i)\sin|\lambda_i t| \,.
\end{aligned}$$

These equations have used the fact that $Real(\mathbf{x}_i) = Real(\overline{\mathbf{x}}_i)$ and $Imag(\mathbf{x}_i) = -Imag(\overline{\mathbf{x}}_i)$. The constants M and N can be chosen to be $M = N$ to get a real solution, but one could choose a constant C such that $M = Ci$ and $N = -Ci$ to produce a real solution with the complex terms of the general solution. We will choose $M = N$, which gives us the general solution

$$\mathbf{w}(t) = 2M(Real(\mathbf{x}_i)\cos|\lambda_i t| - Imag(\mathbf{x}_i)\sin|\lambda_i t|) \,.$$

When we interpret the eigenvectors, it is often that each individual entry of the eigenvector is a pure real or imaginary number. In these cases we can figure out all the surface elevations and velocities signs at a certain time, to make figures of the modes with velocities and surface elevations. If it is put in this form, we can interpret the real parts as amplitudes of positive cosine functions and the imaginary parts as amplitudes of negative sine functions. For the $\mathbf{x}_2$ and $\mathbf{x}_4$ eigenvectors in the constant depths case, we have sums of imaginary and real parts in all the entries of the eigenvectors. These cases give a sum of cosine and sine functions. Since the sine function is 0 at t=0, it is beneficial to take the initial values at that time.

These were special cases, since the eigenspace is of dimension 2 for the $0.0044i$ eigenvalue and $-0.0044i$ eigenvalue. Most of the eigenvectors produced from numerical calculations will have the velocities as pure imaginary numbers, while the surface elevations will be in real numbers. In Fig.6.4, we have the modes that belong to the constant depths four-cell case. We also have arrows that indicate which direction the velocities will be, from the initial time t=0.

The two first eigenvectors correspond to the zero eigenvalues. They produce two linear combinations of two modes, one mode where we have just a constant surface elevation on all the grid cells with zero velocities, and a mode where we have a circular pattern with the velocities (Mode 1). The next two eigenvectors will give us modes (Mode 2 and Mode 3) that move diagonally from cell 1 to cell 3. These modes have the same angular frequency as the two-cell case had. The last mode, Mode 4, moves from cell 1 and 3 to cell 2 and 4. This mode is a motion outwards from the diagonals to the corners opposite in the four cell. This is the fastest mode, a diagonal pulsating mode with angular frequency approximately $\sqrt{2}$ times the Mode 2 and Mode 3 angular frequency. When we change to variable depths, H_1,H_2,$H_3 = 100m$ and $H_4 = 300m$, all the pairs of eigenvalues are distinct and have different modes than the constant depths case. The modes are shown in Fig.6.5. The solutions to the variable depths case are shown in Fig.6.6. If we compare the solutions with constant depths case solutions (Fig.6.3), we notice it is only the V_2 solution which has a constant amplitude, whereas we had many solutions in the constant depths case with constant amplitude. The overall picture of the motions is less harmonic.

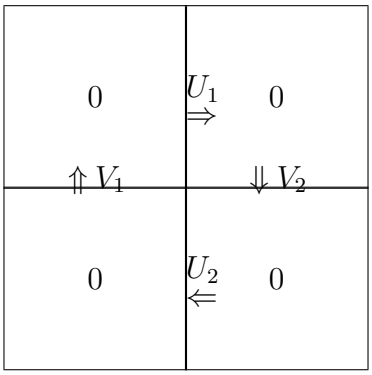

a)Mode 1

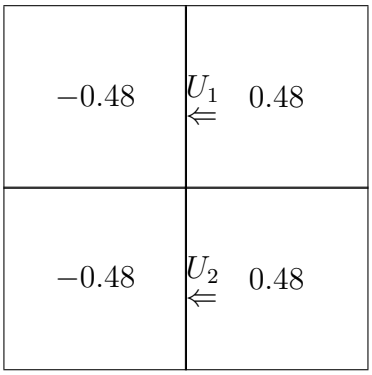

b)Mode 2

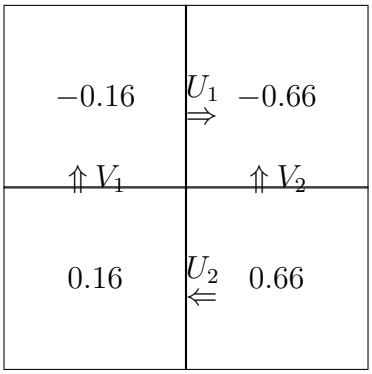

c)Mode 3

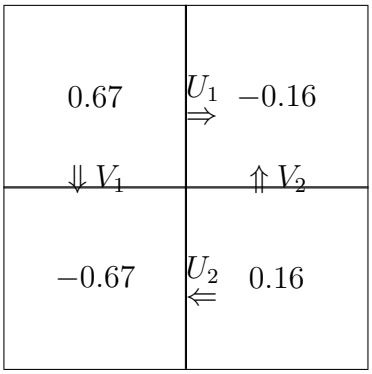

d)Mode 4

Figure 6.5: The modes of the variable depths case $H_1, H_2, H_3 = 100m$ and $H_4 = 300m$ with velocities' directions.

The eigenvalues and eigenvectors for the variable depths case are $\lambda_0 = 0, \lambda_1 = 0, \lambda_2 = 0.0044i, \lambda_4 = 0.0052i, \lambda_6 = 0.0084i$,

$$\mathbf{x}_0 = \begin{pmatrix} -0.08 \\ 0.08 \\ -0.02 \\ 0.08 \\ 0.50 \\ 0.50 \\ 0.50 \\ 0.50 \end{pmatrix}, \mathbf{x}_1 = \begin{pmatrix} -0.02 \\ 0.02 \\ -0.01 \\ 0.02 \\ 0.50 \\ 0.50 \\ 0.50 \\ 0.50 \end{pmatrix}, \mathbf{x}_2 = \begin{pmatrix} 0.21i \\ 0.21i \\ 0 \\ 0 \\ -0.48 \\ 0.48 \\ 0.48 \\ -0.48 \end{pmatrix},$$

$$\mathbf{x}_4 = \begin{pmatrix} -0.09i \\ 0.09i \\ -0.06i \\ -0.24i \\ -0.16 \\ -0.66 \\ 0.66 \\ 0.16 \end{pmatrix}, \mathbf{x}_6 = \begin{pmatrix} -0.10i \\ 0.10i \\ 0.16i \\ -0.04i \\ 0.67 \\ -0.16 \\ 0.16 \\ -0.67 \end{pmatrix}.$$

The modes produced from these eigenvectors are different than the constant depths case. The first modes are constant circular flows belonging to the zero eigenvalues. The difference between the two eigenvectors is that the ratio of the velocities and the surface elevation are different. Secondly, we get modes that are linked to the two-cell case mode, which has the almost the same angular frequency, $w = 0.0044$, and gives us a clear sideways motion. The third mode is more complicated, as one part the flow is going directly from cell 3 to cell 2, and another part which goes past the other cells. Since we had the depth $H_4 = 300m$, between cell 1 and 4, water still goes that way although we had large differences between the surface elevation in cell 3 and 4 for this mode. At last, we have the strongest mode, Mode 4, a mode that spreads out from the diagonal similar to Mode 4 in the constant depths case.

Next, we will check the eigenvectors for the case with the depths $H_1 = 100m, H_2, H_3 = 200m$ and $H_4 = 300m$. We will use this case in the next chapter to study numerical instability, since it has the potential to make the four-cell case solutions more unstable. The eigenvalues and eigenvectors are $\lambda_0 = 0, \lambda_1 = 0, \lambda_2 = 0.0052i, \lambda_4 = 0.0068i, \lambda_6 = 0.0091i$,

$$\mathbf{x}_0 = \begin{pmatrix} 0.07 \\ -0.04 \\ 0.02 \\ -0.04 \\ 0.50 \\ 0.50 \\ 0.50 \\ 0.50 \end{pmatrix}, \mathbf{x}_1 = \begin{pmatrix} 0.20 \\ -0.10 \\ 0.67 \\ -0.10 \\ -0.48 \\ -0.48 \\ -0.48 \\ -0.48 \end{pmatrix}, \mathbf{x}_2 = \begin{pmatrix} -0.21i \\ 0.14i \\ -0.02i \\ 0.05i \\ -0.52 \\ 0.61 \\ 0.33 \\ -0.42 \end{pmatrix},$$

$$\mathbf{x}_4 = \begin{pmatrix} -0.01i \\ 0.06i \\ -0.01i \\ -0.02i \\ -0.42 \\ -0.52 \\ 0.66 \\ 0.28 \end{pmatrix}, \mathbf{x}_6 = \begin{pmatrix} 0.08i \\ -0.12i \\ -0.13i \\ 0.07i \\ -0.51 \\ 0.25 \\ -0.41 \\ 0.68 \end{pmatrix}.$$

When we have increased variability of the depths, we have greater variation in the components in the eigenvectors. Bearing this in mind, we should expect a chaotic motion compared to the other four cell cases. The modes to this case shown in Fig.6.7, confirm this property. What has changed is that the Mode 2 velocities are no longer a pure two-cell motion, we have velocities in the y-direction as well. Mode 4 appears to be different, however the signs are just reversed on the elevations, giving us the opposite direction on all the velocities. Depicted on Fig.6.8, are the solutions of this case, with only $\eta_4 = 0$ initially.

If we choose one of the eigenvectors and evaluate the scalar product with the initial eigenvector and the solution in Eqn.6.2, we will produce the Fourier coefficient for that particular eigenvector

$$c_i(t) = \frac{\langle \sum_{i=0}^{7} d_i \mathbf{x}_i(t) e^{\lambda_i t}, \mathbf{x}_i(0) \rangle}{\langle \mathbf{x}_i(0), \mathbf{x}_i(0) \rangle}. \tag{6.3}$$

When we have a complex conjugate to the eigenvector, we will use the average of the normal and the conjugate eigenvector, $\frac{(\mathbf{x}_i(0) + \overline{\mathbf{x}}_i(0))}{2}$, instead of $\mathbf{x}_i(0)$ in the calculation of $c_i(t)$. Since λ_i in general has a small real part that does not grow, we will ignore it with respect to the Fourier coefficient, as it is close to zero. Moreover, the difference between the eigenvectors $\mathbf{x}_i(0) - \mathbf{x}_i(t)$ is also negligible. The absolute value of c_i is constant as time increases in the linear case. We will refer to this for comparison of the non-linear case, in next chapter. The total energy of the linear four-cell case (Eqn.3.4) is almost constant, and is on the machine level of accuracy like the three-cell case, with the same energy. This is as expected, since the initial values are one cell with 1m surface elevation and no velocities. Summing up this chapter, we have seen the modes of the four-cell linear case and how they change with different depths. In the next chapter, we will discuss how the non-linear term affects the four-cell case.

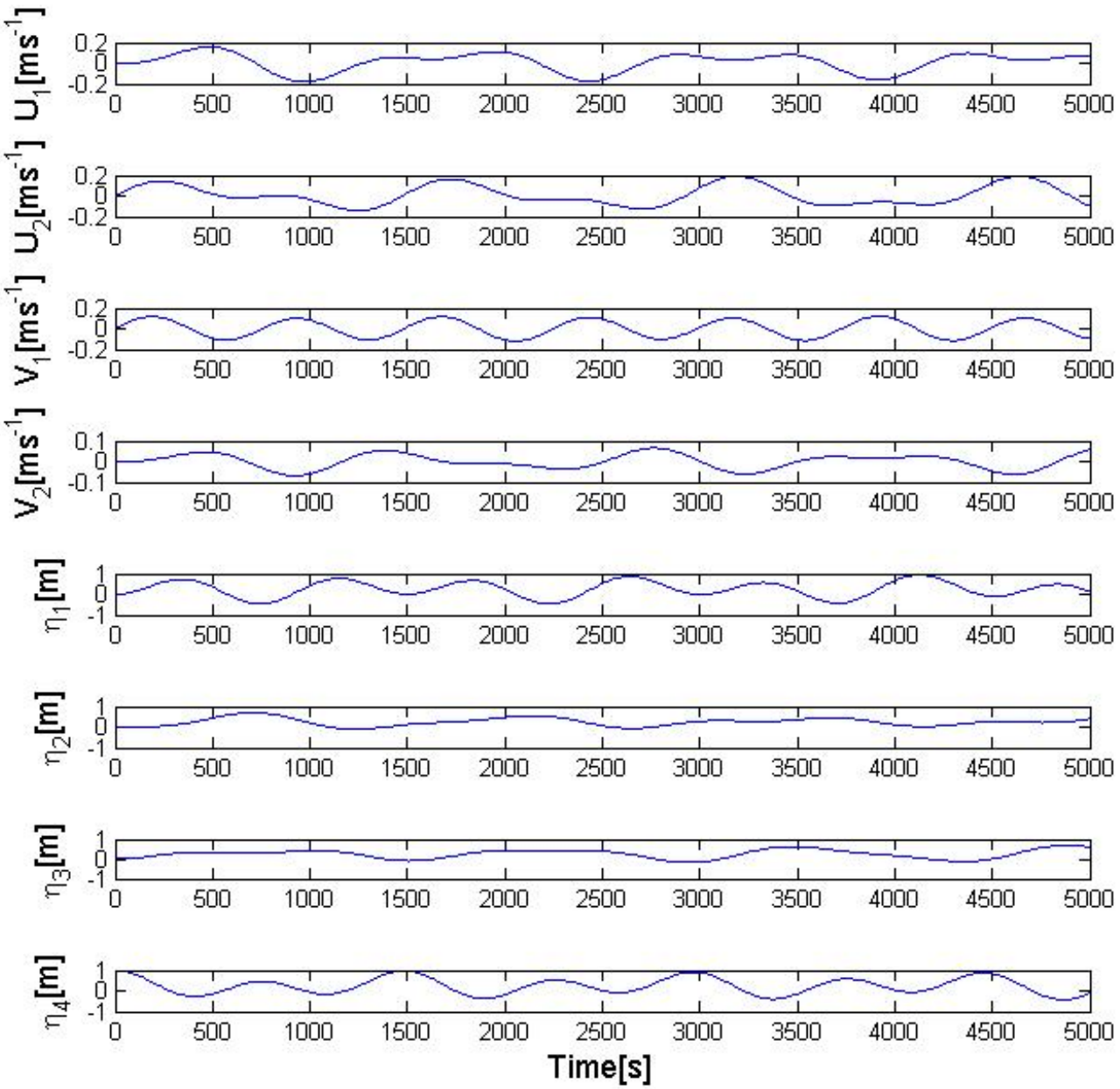

Figure 6.6: The solutions for the variable depths case, $H_4 = 300m$, only η_4 is non-zero initially.

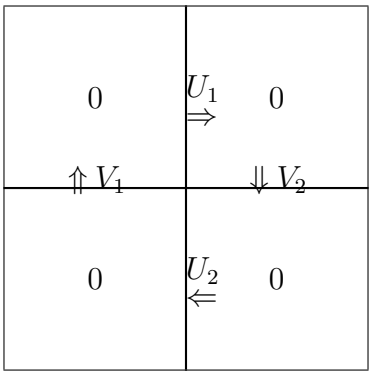

$d)Mode\,1$

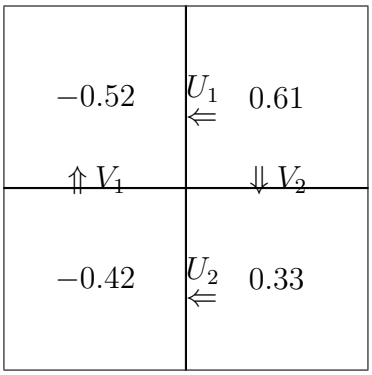

$d)Mode\,2$

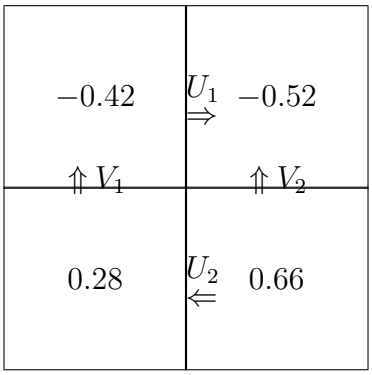

$d)Mode\,3$

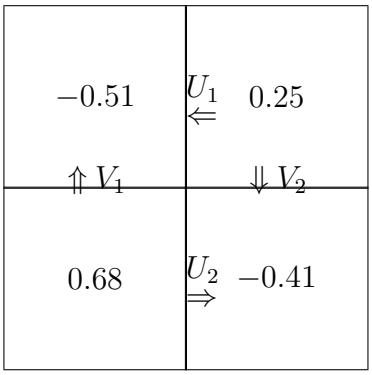

$d)Mode\,4$

Figure 6.7: The modes of the $H_1 = 100m, H_2, H_3 = 200m$ and $H_4 = 300m$ case with velocities directions.

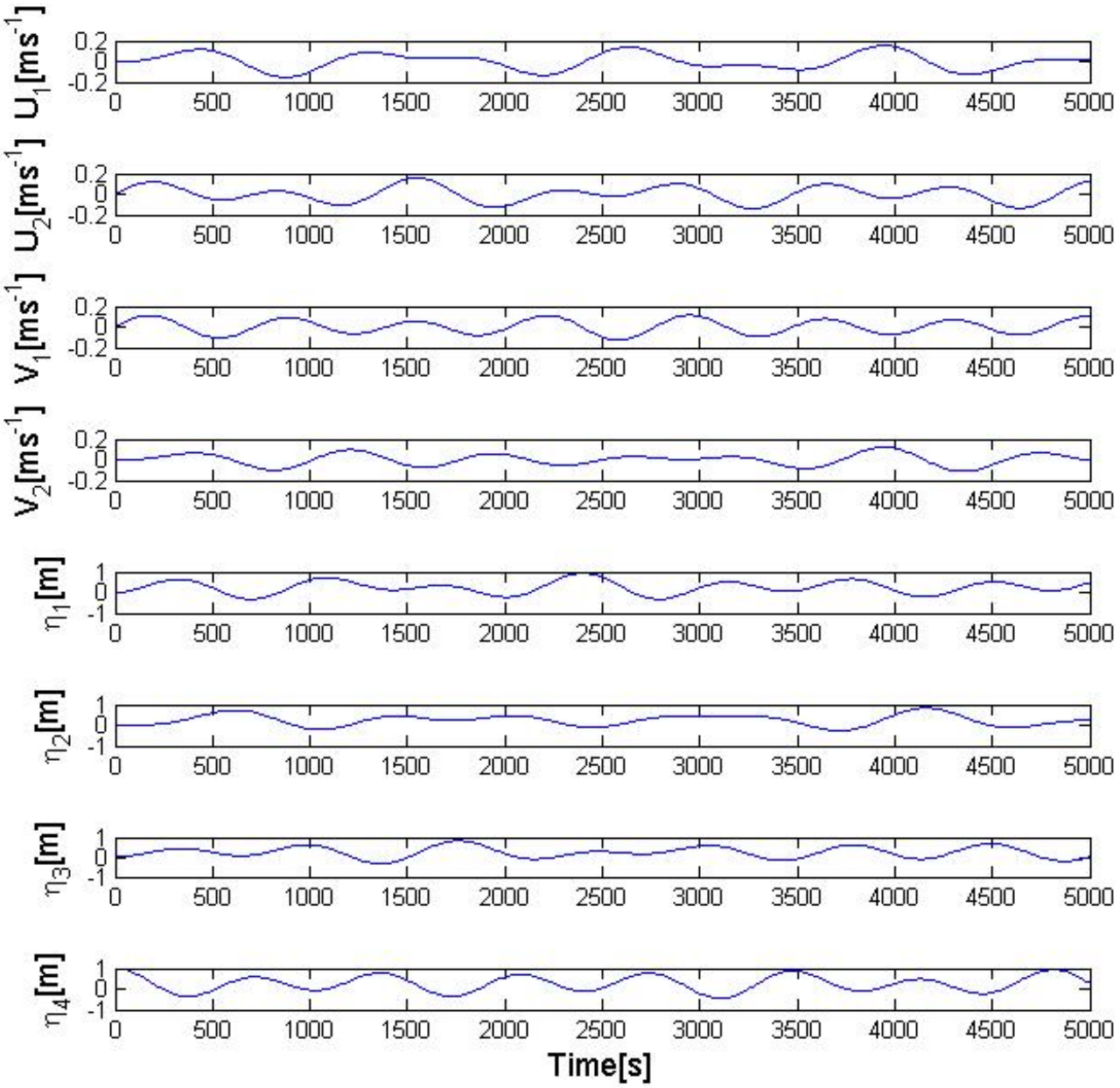

Figure 6.8: Solutions of the linear variable depths case, $H_1 = 100m, H_2, H_3 = 200m$ and $H_4 = 300m$. Initial surface elevation is 1m at η_4, and the rest of the initial values are 0.

Chapter 7

The non-linear four-cell case

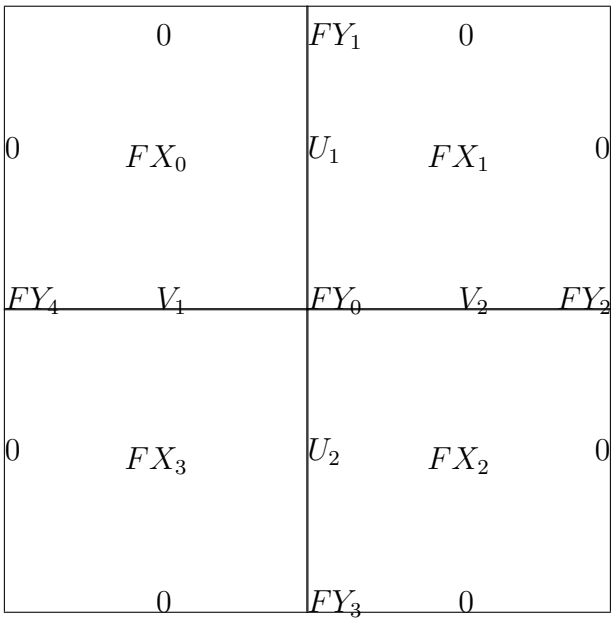

Figure 7.1: Variables of the non-linear four-cell advective and flux form discretization.

In the non-linear four-cell case, we will calculate the non-linear terms by adding together the contributions from the surrounding four sides. These contributions are called transportive fluxes. Moreover, the non-linear terms will be calculated by linearly interpolated velocities at the depth-averaged velocity points U_1, U_2, V_1, V_2 . The four surrounding non-linear terms are evaluated by the advective form expressed in Eqn.4.1, and flux form found in Eqn.4.2. Surprisingly, we will see that these two forms have equal total non-linear terms. We set up the calculations of the four non-linear terms by using Fig.7.1, for both the advective and flux forms.

The non-linear terms for U_1 in advective form are

$$\begin{aligned} FY_1 &= 0\,, \\ FY_0 &= \frac{(V_1+V_2)(U_1+U_2)}{4}\,, \\ FX_0 &= \frac{U_1(U_1)}{2}\,, \\ FX_1 &= \frac{U_1(U_1)}{2}\,, \end{aligned} \tag{7.1}$$

and non-linear terms in the flux form for U_1 are

$$\begin{aligned} FY_1 &= 0\,, \\ FY_0 &= \frac{(V_1+V_2)(U_1+U_2)}{4}\,, \\ FX_0 &= \frac{U_1^2}{4}\,, \\ FX_1 &= \frac{U_1^2}{4}\,. \end{aligned} \tag{7.2}$$

Both these sets of equations, Eqn.7.1 and Eqn.7.2, give the same total non-linear term for U_1,

$$F_{tot} = FX_1 - FX_0 + FY_1 - FY_0 = -\frac{(V_1+V_2)(U_1+U_2)}{4}\,.$$

The discretization for the derivative of depth-averaged velocity component U_1 is then

$$\frac{dU_1}{dt} = -\frac{F_{tot}}{\Delta y} - \frac{g\Delta\eta}{\Delta x}\,.$$

Repeating this discretization for all the depth-averaged velocity points, we obtain the system of equations

$$\begin{aligned} \frac{dU_1}{dt} &= -g\frac{\eta_2-\eta_1}{\Delta x} + \frac{(V_1+V_2)(U_1+U_2)}{4\Delta y}\,, \\ \frac{dU_2}{dt} &= -g\frac{\eta_3-\eta_4}{\Delta x} - \frac{(V_1+V_2)(U_1+U_2)}{4\Delta y}\,, \\ \frac{dV_1}{dt} &= -g\frac{\eta_1-\eta_4}{\Delta y} - \frac{(V_1+V_2)(U_1+U_2)}{4\Delta x}\,, \\ \frac{dV_2}{dt} &= -g\frac{\eta_2-\eta_3}{\Delta y} + \frac{(V_1+V_2)(U_1+U_2)}{4\Delta x}\,, \\ \frac{d\eta_1}{dt} &= -H_1\frac{U_1}{\Delta x} + H_4\frac{V_1}{\Delta y}\,, \\ \frac{d\eta_2}{dt} &= H_1\frac{U_1}{\Delta x} + H_2\frac{V_2}{\Delta y}\,, \\ \frac{d\eta_3}{dt} &= H_3\frac{U_2}{\Delta x} - H_2\frac{V_2}{\Delta y}\,, \\ \frac{d\eta_4}{dt} &= -H_3\frac{U_2}{\Delta x} - H_4\frac{V_1}{\Delta y}\,. \end{aligned} \tag{7.3}$$

Put into matrix form, this system of equations is expressed $\frac{d}{dt}\mathbf{w}(t) = A\mathbf{w}(t)$ where A is

$$\begin{pmatrix} 0 & 0 & \frac{(U_1+U_2)}{4\Delta y} & \frac{(U_1+U_2)}{4\Delta y} & \frac{g}{\Delta x} & -\frac{g}{\Delta x} & 0 & 0 \\ 0 & 0 & -\frac{(U_1+U_2)}{4\Delta y} & -\frac{(U_1+U_2)}{4\Delta y} & 0 & 0 & -\frac{g}{\Delta x} & \frac{g}{\Delta x} \\ -\frac{(V_1+V_2)}{4\Delta x} & -\frac{(V_1+V_2)}{4\Delta x} & 0 & 0 & -\frac{g}{\Delta x} & 0 & 0 & \frac{g}{\Delta x} \\ \frac{(V_1+V_2)}{4\Delta x} & \frac{(V_1+V_2)}{4\Delta x} & 0 & 0 & 0 & -\frac{g}{\Delta y} & \frac{g}{\Delta y} & 0 \\ -\frac{H_1}{\Delta x} & 0 & \frac{H_4}{\Delta y} & 0 & 0 & 0 & 0 & 0 \\ \frac{H_1}{\Delta x} & 0 & 0 & \frac{H_2}{\Delta y} & 0 & 0 & 0 & 0 \\ 0 & \frac{H_3}{\Delta x} & 0 & -\frac{H_2}{\Delta y} & 0 & 0 & 0 & 0 \\ 0 & -\frac{H_3}{\Delta x} & -\frac{H_4}{\Delta y} & 0 & 0 & 0 & 0 & 0 \end{pmatrix}.$$

We wrote A in this way to find a skew-symmetric form, but this is not the case for this four cell system. It is not easy to see how this matrix can become skew-symmetric, even for the constant depths case. However, we have volume conservation, and this property is probably the cause of the numerical stability we will later observe. The numerical solution of Eqn.7.3, we get by setting $\Delta x = \Delta y = 10000m$ H_1,H_2,H_3, $H_4 = 100m$ and

$$\mathbf{w}(0) = \begin{pmatrix} 0 \\ 0 \\ 0 \\ 0 \\ 0 \\ 0 \\ 0 \\ 1 \end{pmatrix},$$

has a similar solution as the linear case. There are differences in the solutions of $O(10^{-3})$, as shown in Fig.7.2. The differences in the surface elevations and velocities of the non-linear terms do not give any growth over time, and over longer time periods we can produce envelopes for all the solutions. In Fig.7.3, we observe that the eigenvalues are of $O(10^{-18})$ in the real value part. The eigenvalues have real part equal to machine error, as we had for all the linear cases. Even though the matrix A is not skew-symmetric. The Fourier coefficients have constant amplitudes for the constant depths case as shown in Fig.7.4. This means that we have stable solutions, however the stability changes when we have variable depths.

We set H_1,H_2,$H_3 = 100m$ and $H_4 = 300m$. Shown in Fig.7.5, the eigenvalues have real value part of $O(10^{-6})$. The smallest non-zero eigenvalues, λ_2 and λ_3, have machine level precision on the real part, so we have a large real part for all of the eigenvalues. The longest oscillation is the most numerical stable in this variable depths case. The Fourier coefficients are also changed, they are no longer of constant amplitude but have formed weak envelopes for the c_{λ_1} solution, as shown in Fig.7.6. The total energy of the constant depths non-linear case is not constant, as we observe in Fig.7.7. It is in fact forming envelopes, thus the non-linear energy does not grow uncontrollably. The energy for the case H_1,H_2,$H_3 = 100m$ and $H_4 = 300m$ is oscillating on a larger scale than the constant depths case, as portrayed in Fig.7.8.

For the case with $H_1 = 100m, H_2, H_3 = 200m$ and $H_4 = 300m$, the eigenvalues (Fig.7.9) are in almost the same real value range as the previous variable depths case. The notable exception is that the smallest non-zero eigenvalue now has a real part of $O(10^{-6})$. Furthermore, we observe that the Fourier coefficients form a greater amount of envelopes in this case, as shown in Fig.7.10. In this chapter, we have observed that the non-linear four-cell case had machine error of the eigenvalues for the constant depths case. When we changed to variable depths the real value parts became larger, and we had less stable solutions.

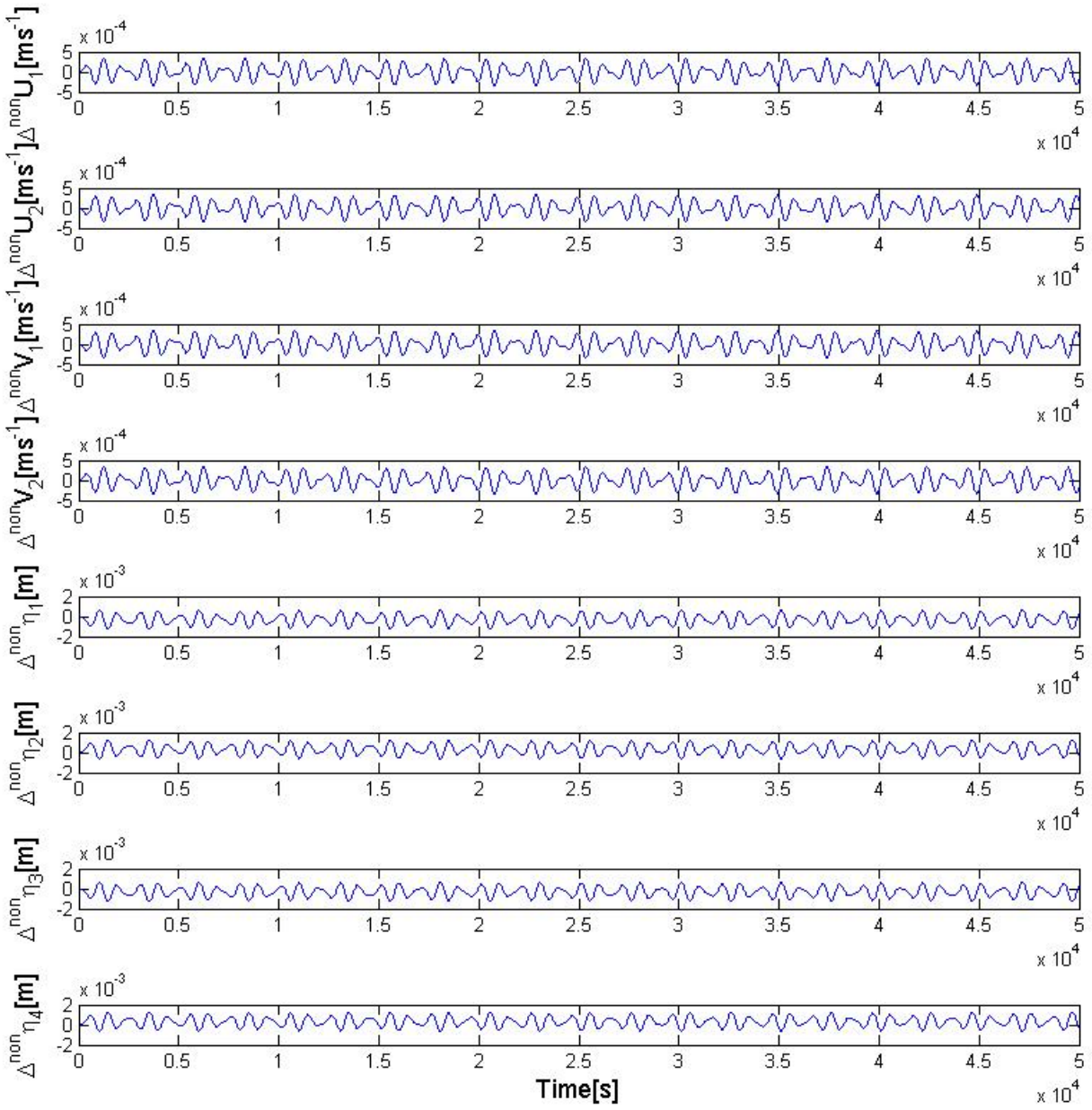

Figure 7.2: The differences of the solutions of the non-linear constant depths four-cell case and the linear case. Δ^{non} means difference of the variable from non-linear to linear. The time span is 50000s.

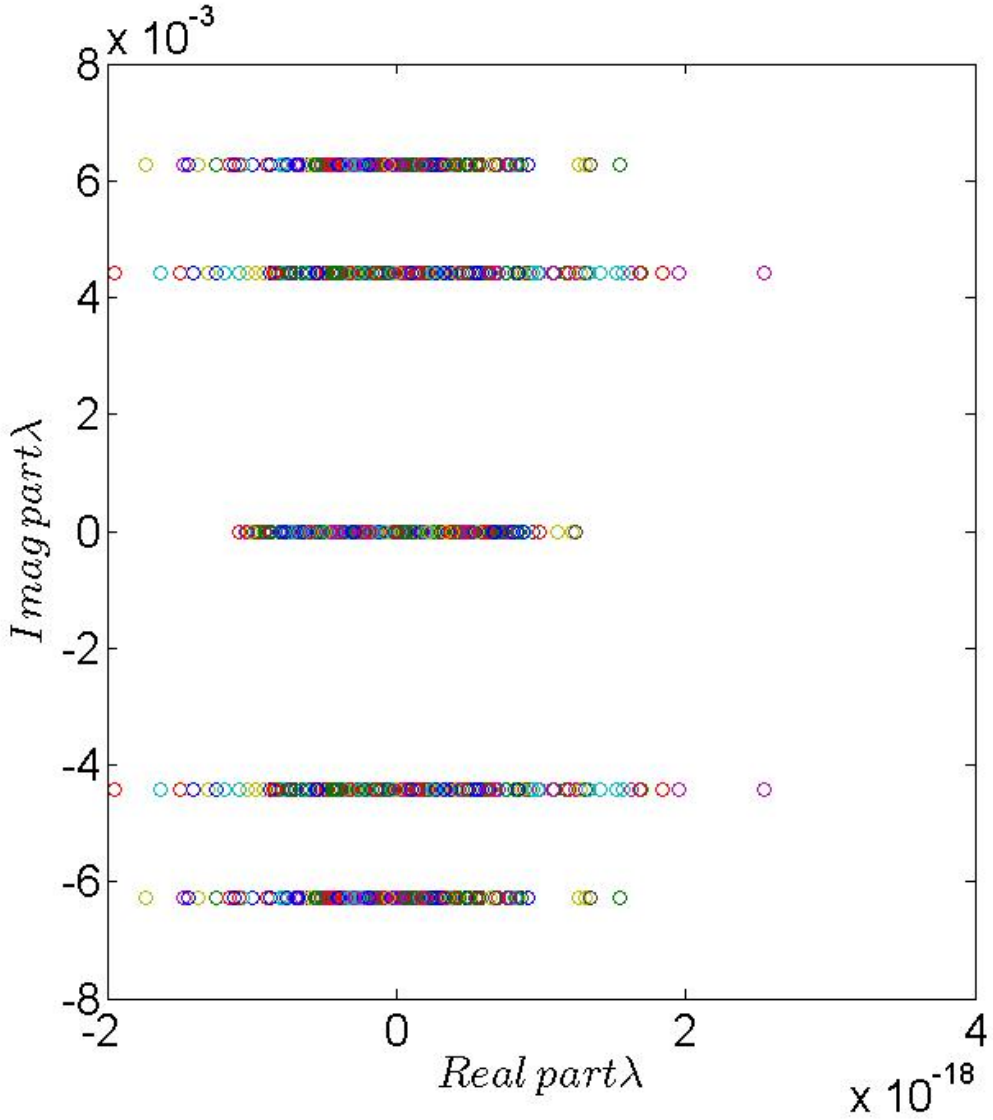

Figure 7.3: The eigenvalues of the non-linear four cell with constant depths, only η_4 is non-zero initially. Notice the real part is $O(10^{-18})$.

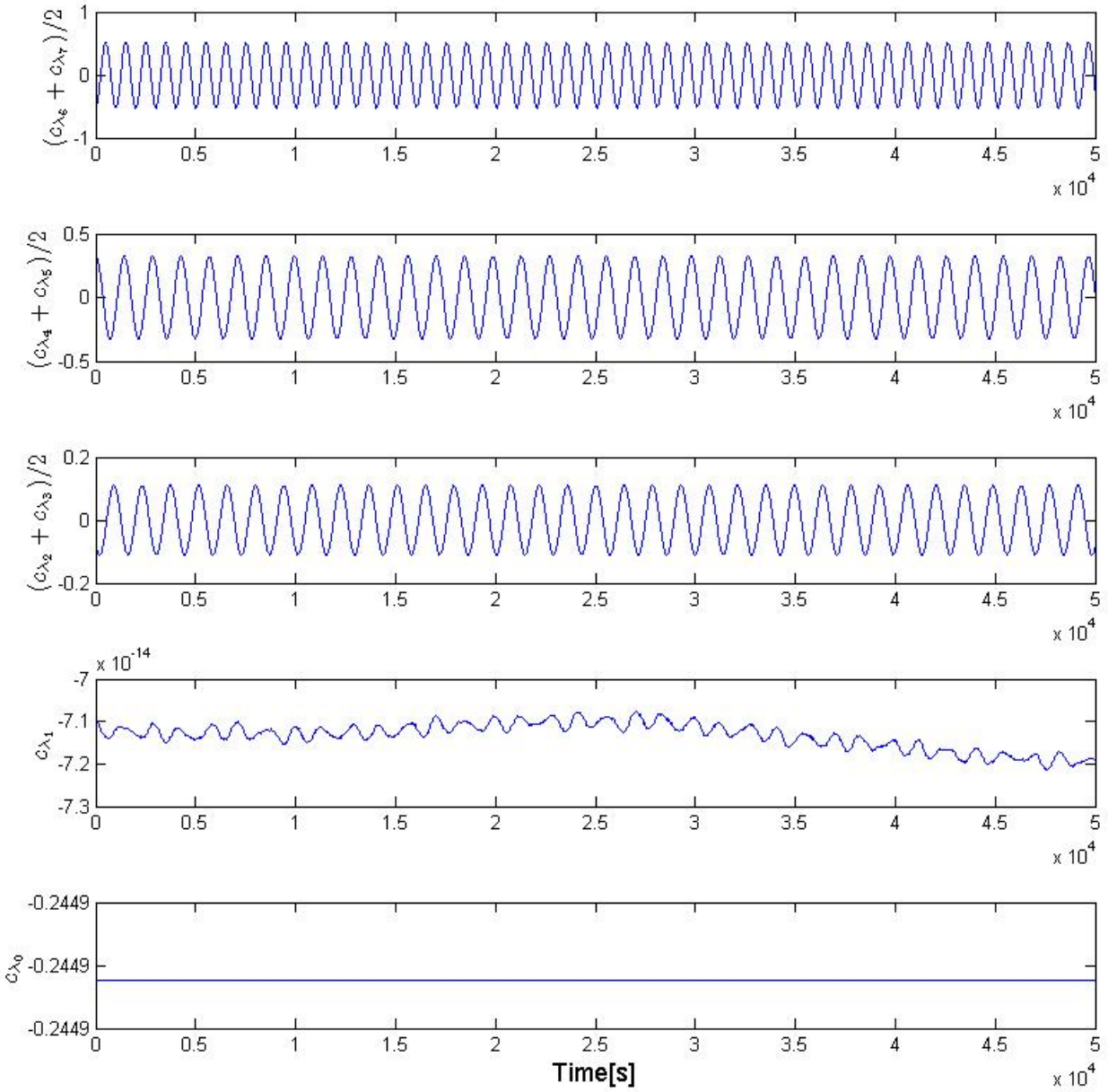

Figure 7.4: The Fourier coefficients of the case H_1,H_2,H_3,$H_4 = 100m$, time span 50000s.

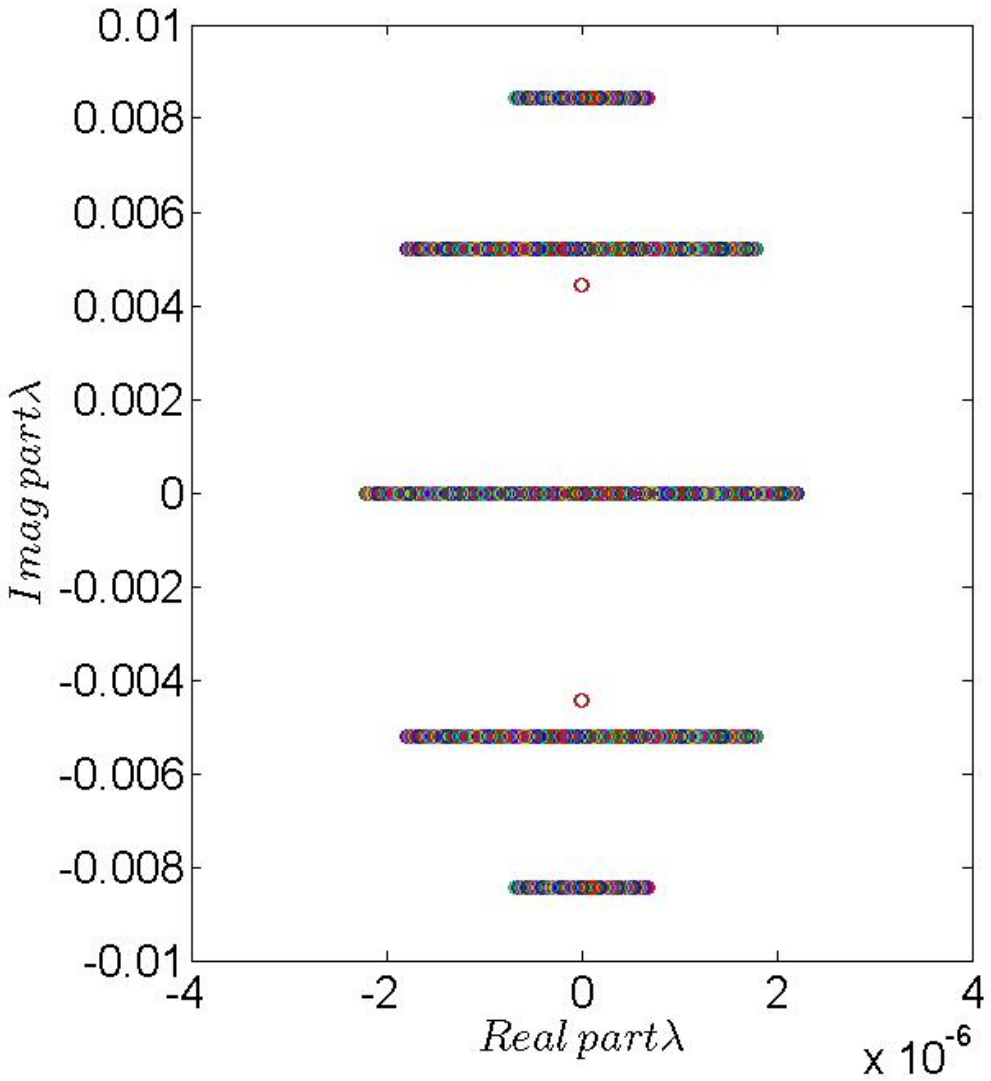

Figure 7.5: Non-linear variable depths case eigenvalues, H_1,H_2,$H_3 = 100m$ and $H_4 = 300m$.

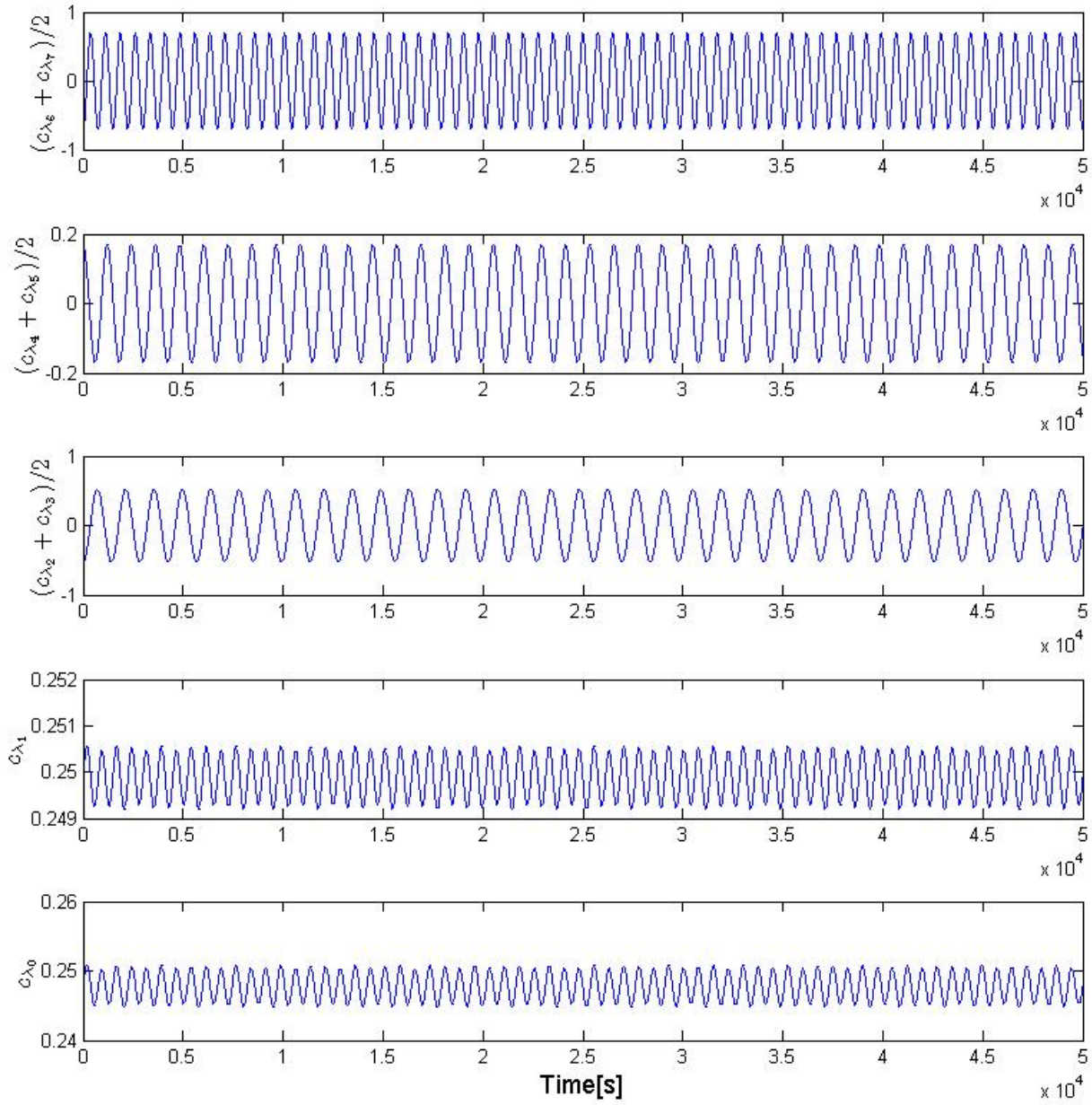

Figure 7.6: The Fourier coefficients of the case H_1,H_2,$H_3 = 100m$ and $H_4 = 300m$, the time span is 50000s to notice the envelopes.

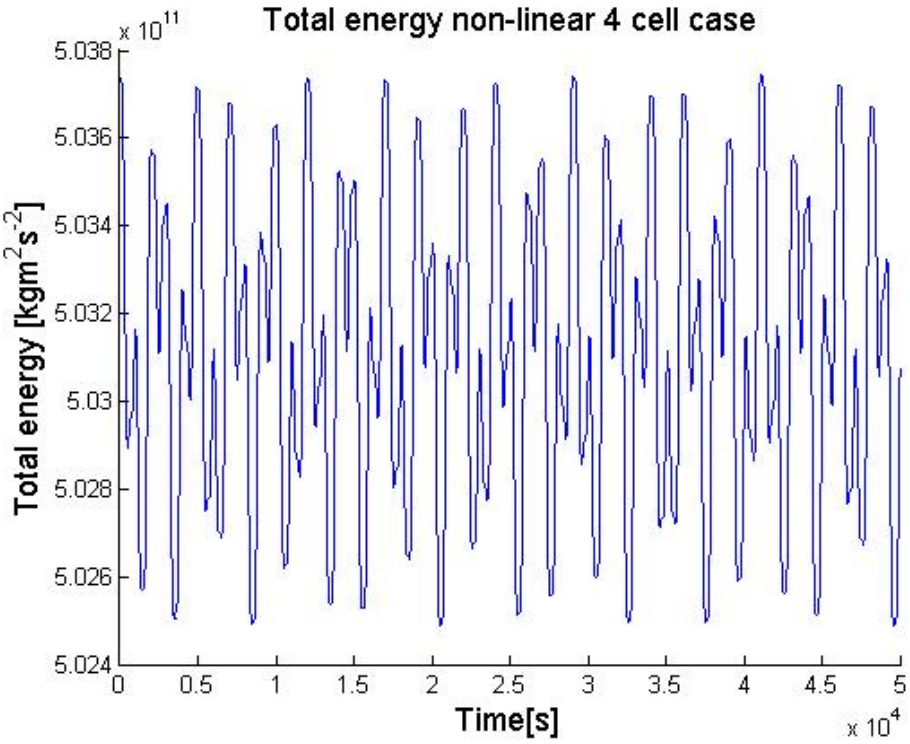

Figure 7.7: Total energy of the constant depths non-linear 4 cell case, 50000s time period.

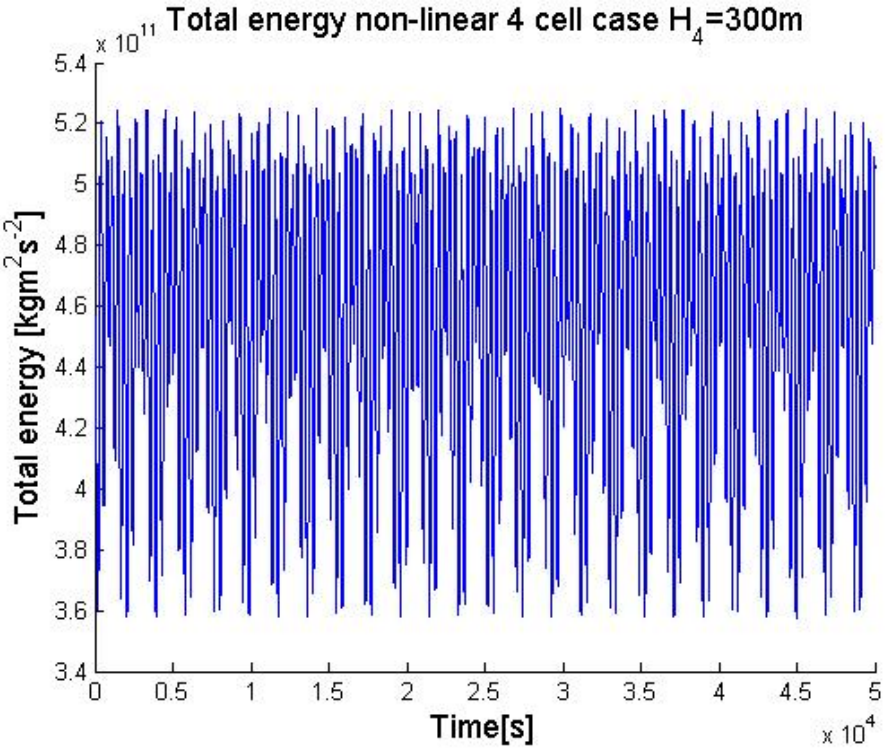

Figure 7.8: Total energy of the the case H_1,H_2,$H_3 = 100m$ and $H_4 = 300m$, 50000s time period.

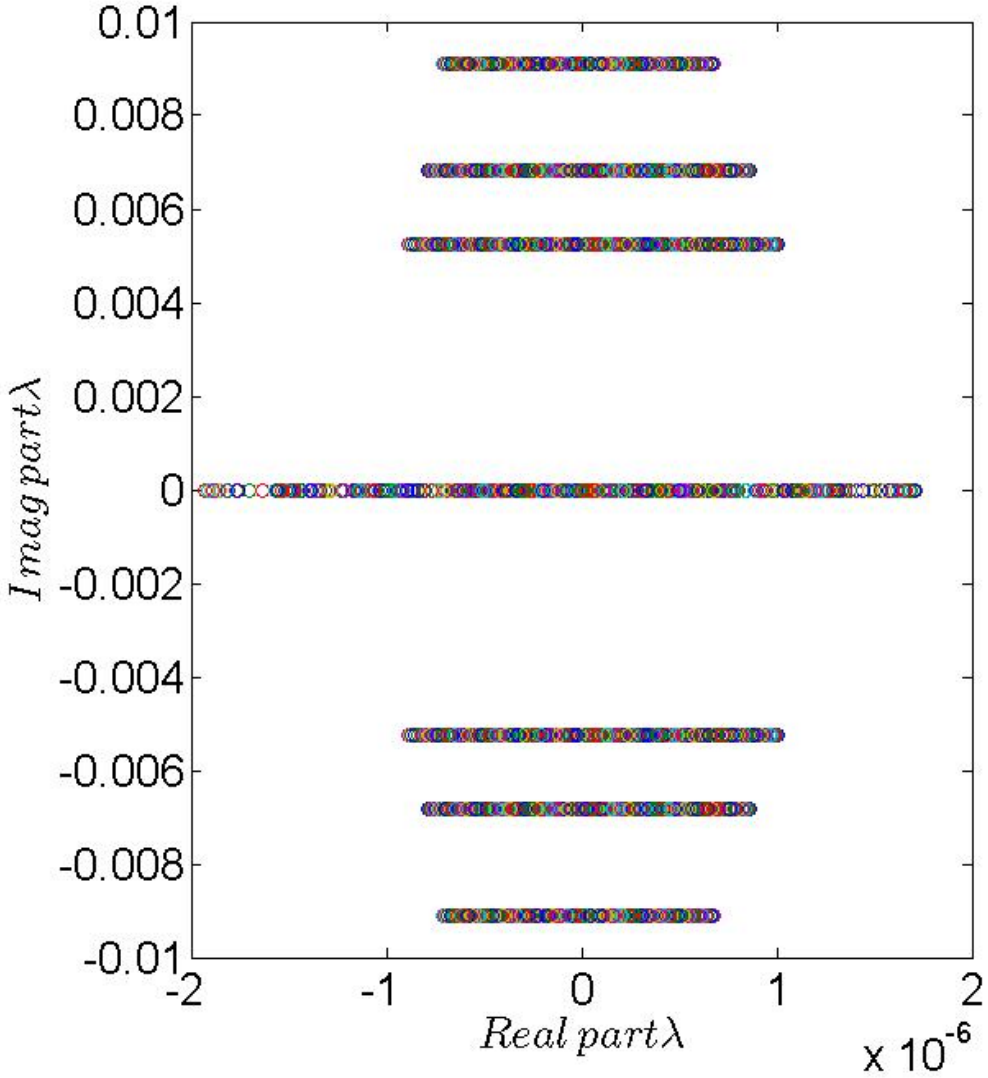

Figure 7.9: The eigenvalues of the case $H_1 = 100m, H_2, H_3 = 200m$ and $H_4 = 300m$.

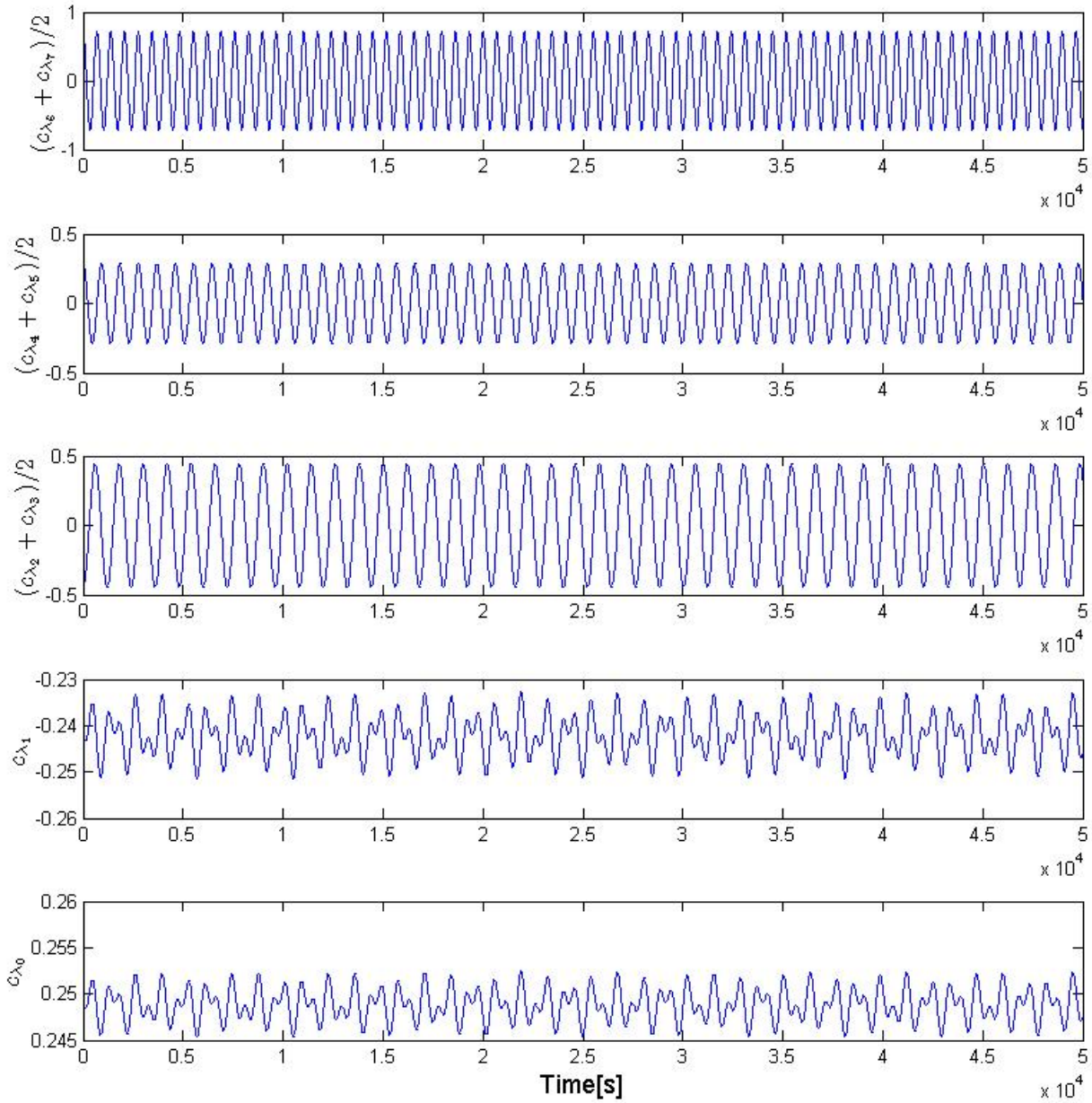

Figure 7.10: The Fourier coefficients of the case $H_1 = 100m, H_2, H_3 = 200m$ and $H_4 = 300m$, 50000s time span.

Chapter 8

Conclusion

In this project I have found out various properties of the two, three and four celled Arakawa C-grids and schemes used to model the change of the surface elevations and depth-averaged velocity in the cells. I have studied the eigenvalues to understand the changes from the continuous case to the discrete case, as well as the accuracy of the eigenvalues in different numerical schemes. Linked to the eigenvalues are the modes of the various cells. The modes of the different cells required some effort to understand, especially the four cell modes. The four cell modes contained various patterns of flows, as they had two dimensional flow. In the two and three cell cases, there were only flows in one horizontal direction.

Then main motivation for this project was to study energy conserving methods of the Arakawa C-cells, by examining the eigenvalues of various propagation matrices corresponding to discretized systems of the shallow water equations. In some cases, the real part of the eigenvalues was at the machine level error. In other cases, where I failed to produce a skew-symmetric matrix, I got relative large real parts which gave growth in the solutions over time. One of the surprising results was that it was possible to combine the advective and flux form equations into a more stable form for the non-linear three-cell case, a skew-symmetric form, but this property was not generalized to the variable depths case in a rigorous fashion. I could not create a skew-symmetric non-linear three-cell variable depths system that worked for all the possible depths.

In the non-linear four-cell constant depths case, there was not an obvious way to make the matrix skew-symmetric, as one could do in the non-linear constant depths three-cell case. However, there was volume conservation in this system, which also gave numerical stability. To make gains beyond this thesis, it would be fruitful to find a discretization that makes the non-linear three- and four-cell variable depths case more stable.

Is it still possible to find a way to make the non-linear variable depths case stable? There is an energy method described by (Lilly, 1965) that finds invariants in the discrete Fourier domain. The large computational stencils of these energy methods produce can be rather complicated, as shown in (Navon, 1981) and (Sasaki, 1976).

For the four cell case I have chosen a different structure than the three- and two-cell cases to get terms in the y-directions. If I instead had all the cells in the four-cell case in the x-direction, the average of advective and flux form propagation matrix is similar to a skew-symmetric matrix. This is also true for the n-th cell case as well.

Another aspect is that I neglected the Coriolis virtual force, which is an effect that is present in the shallow water equations when one deals with large length or time scales. In (Adcroft et al., 1999) a combination of C- and D-grids are used in high and low resolution to deal with Coriolis. In (Espelid et al., 2000) a energy conserving method is found to weight the Coriolis parameter for variable depths. The method used for the Coriolis effect in this paper could give inspiration to accurately deal with the non-linear variable depths cases in this master thesis.

Appendix A

List of symbols

A	Propagation matrix
$\tilde{A}$	Non-linear part of propagation matrix
B	Linear part of propagation matrix
c_{λ_i}	i-th Fourier coefficient of λ_i
C	Weighted propagation matrix
D	Diagonal matrix
Δ^{non}	Difference of the variable from non-linear to linear
η	Surface elevation
η_i	Surface elevation at i-th cell
E_{pot}	Potential energy
E_{kin}	Kinetic energy
E_{tot}	Total energy
$\mathbf{f}$	Body force vector
f	The Coriolis parameter
F_{tot}	Total non-linear term
FX_0, FX_1	Non-linear terms, transportive fluxes
FX_2, FX_3	Non-linear terms, transportive fluxes
FY_0, FY_1, FY_2	Non-linear terms, trasportive fluxes
FY_3, FY_4	Non-linear terms, trasportive fluxes
g	Gravity
H	Mean depth
H_i	Mean depth at velocity point
H_u	Mean depth at U-point
H_v	Mean depth at V-point
h	Total depth $(H + \eta)$
L	Length of the body of water
P	Pressure
∇p	Pressure gradient force
π	Pi
ρ	Fluid density
t	Time
τ	Deviatoric stress tensor
μ	Viscosity
$\mathbf{u}'$	Depth-varying component of the horizontal velocities vector
$\mathbf{u}$	Depth-averaged component of the horizontal velocities vector
$\mathbf{U} = (U, V)$	Horizontal depth-averaged velocities vector
U	Horizontal depth-averaged velocity component in the $x-$direction
U_i	Horizontal depth-averaged velocity component in the $x-$direction, i-th cell
U_{if}	i-th horizontal depth-averaged velocity component in the $x-$direction, flux form

U_{ia}	i-th horizontal depth-averaged velocity component in the $x-$direction, advective form
U_{il}	i-th horizontal depth-averaged velocity component in the $x-$direction, linear case
U_{in}	i-th horizontal depth-averaged velocity component in the $y-$direction, non-linear case
V	Horizontal depth-averaged velocity component in the $y-$direction
V_i	Horizontal depth-averaged velocity component in the $y-$direction, i th cell
V_{if}	i-th horizontal depth-averaged velocity component in the $y-$direction, flux form
V_{ia}	i-th horizontal depth-averaged velocity component in the $y-$direction, advective form
V_{il}	i-th horizontal depth-averaged velocity component in the $y-$direction, linear case
V_{in}	i-th horizontal depth-averaged velocity component in the $y-$direction, non-linear case
$\mathbf{w}(t)$	The solution vector
w	Angular frequency
x	x-coordinate
y	y-coordinate
z	z-coordinate
ζ	Volume viscosity

Bibliography

Adcroft, A., Hill, C., and Marshall, J. (1999). A new treatment of the Coriolis terms in C-grid models at both high and low resolutions. *Monthly Weather Review*, 127(8):1928–1936.

Arakawa, A. and Lamb, V. R. (1977). Computational design of the basic dynamical processes of the UCLA general circulation model. *Methods in computational physics*, 17:173–265.

Espelid, T. O., Berntsen, J., and Barthel, K. (2000). Conservation of energy for schemes applied to the propagation of shallow-water inertia-gravity waves in regions with varying depth. *International Journal for Numerical Methods in Engineering*, 49(12):1521–1545.

Haidvogel, D. B. and Beckmann, A. (1999). Numerical ocean circulation modeling.

Horn, W., Mortimer, C. H., and Schwab, D. J. (1986). Wind-induced internal seiches in Lake Zurich observed and modeled. *Limnol. Oceanogr*, 31(6):1232–1254.

Kundu, P. K. and Cohen, I. M. (2008). Fluid mechanics. 4th.

Lilly, D. K. (1965). On the computational stability of numerical solutions of time-dependent non-linear geophysical fluid dynamics problems. *Monthly Weather Review*, 93(1):11–25.

Mesinger, F. and Arakawa, A. (1976). Numerical methods used in atmospheric models, volume 1. In *Global Atmospheric Research Program World Meteorological Organization, Geneva (Switzerland).*, volume 1.

Navon, I. (1981). Implementation of a posteriori methods for enforcing conservation of potential enstrophy and mass in discretized shallow-water equations models. *Monthly Weather Review*, 109(5):946–958.

Rabinovich, A. B. (2009). Seiches and harbor oscillations. *Handbook of coastal and ocean engineering*, pages 193–236.

Reddy, J. N. (2013). *An introduction to continuum mechanics*. Cambridge University Press.

Sasaki, Y. K. (1976). Variational design of finite-difference schemes for initial value problems with an integral invariant. *Journal of Computational Physics*, 21(3):270–278.

Wubber, C. and Krauss, W. (1979). The two dimensional seiches of the Baltic Sea. *Oceanologica Acta*, 2(4):435–446.